Computers and Geotechnics 152 (2022) 105037

Contents lists available at ScienceDirect

Computers and Geotechnics

journal homepage: www.elsevier.com/locate/compgeo

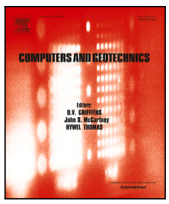

Research paper

Molecular dynamics modeling of cracks in dry clay sheets at the nanoscale

Zhe Zhang, Xiaoyu Song *

Department of Civil and Coastal Engineering, University of Florida, Gainesville, FL, United States of America

ARTICLE INFO

Keywords:
Molecular dynamics
Cracking
Clay
Single sheet
Nanoscale

ABSTRACT

Clay is a nanomaterial by nature. The cracking in clay at the nanoscale can provide significant insight into the cracking mechanism in clay at the continuum scale. This article is devoted to understanding the atomic-scale mechanism of the formation of cracks in a dry clay sheet through molecular dynamics with a general force field for clay. We simulate the formations of mode I and mode II cracks in intact dry clay sheets under tension and shear loading conditions, respectively. The numerical results show that the mode I and II cracking in a clay sheet is brittle and strain-rate dependent. The notion of critical bond stretch is adopted to model the breakage of bonds between atoms in clay. The critical bond length for crack formation is determined by the radial distribution function and the force curve between a pair of atoms. We investigate the crack initiation under mode I and mode II loading conditions from the bond breakage analysis. We interpret the cracking mechanism in terms of the type and number of broken bonds in mode I and mode II cracking. We present the stress intensity factor and cracking energy release rate under both cracking modes. The numerical results of the stress intensity factor and cracking energy release rate are quantitatively comparable to the experimental and numerical data in the literature.

1. Introduction

Cracking in clay at multiple length scales is an issue in geotechnical engineering (e.g., Terzaghi et al., 1996; Lambe and Whitman, 1991; Mitchell and Soga, 2005; Miller et al., 1998; Alonso, 2021; Menon and Song, 2022a,b). For instance, cracks in clay could be a precursor to natural slope failure (Thusyanthan et al., 2007; Lu and Godt, 2013). The crack in clay could significantly decrease the strength of clay that could trigger slope failure (Lu and Dong, 2017). Cracks in clay could provide preferential flow paths for fluids and enhance hydraulic conductivity. The increase in hydraulic conductivity due to fracturing could induce severe damages in the clay barrier system (Li et al., 2016; Lu and Kaya, 2013; Niu et al., 2020). Numerous studies of cracking in clay were focused on the continuum or field scales (e.g., Ayad et al., 1997; Kodikara et al., 2020; Lisjak et al., 2014; Menon and Song, 2019, among others). Physical experiments have been carried out to investigate cracks in soil (Hanson et al., 1994; Hallett and Newson, 2001). Clay is a nanomaterial by nature. Clays usually appear in the form of aggregates of tiny crystals of size smaller than 2μm (Mitchell and Soga, 2005). Because of their fine-grained polycrystalline nature, laboratory measurements of clay's structural and mechanical properties including cracking are quite challenging (Wang et al., 2001; Ortega et al., 2007; Likos et al., 2019). Cracks in clay at the nanoscale could move discretely in the atomic lattice through breakage of atomic bonds (Abraham et al., 1997). Indeed, cracking in clay is a multiscale problem. The knowledge of cracking in a clay platelet at the nanoscale could provide significant insight into the formation of cracks in clay at the continuum scale. For instance, the cracking in clay at the continuum scale can propagate across clay platelets (i.e., cracking orthogonal to the 001 plane) or between clay platelets (i.e., cracking parallel to the 001 plane) under certain loading conditions. For the former case, the cracking mechanism of a single clay platelet could be critical to interpret and characterize the cracking process in clay at the continuum scale. The micro-scratch testing of shale samples in Akono and Kabir (2016) showed that the fracture toughness at microscale is several orders of magnitude larger than the results at macroscale. The cracking in a clay platelet could help understand the formation of cleavage planes and edge charges of clay minerals (Mitchell and Soga, 2005). In this study, we investigate the nanoscale cracking mechanism in a dry clay sheet under mechanical loading through molecular dynamics with a general clay force field. Next, we briefly review the MD modeling of the mechanical properties and failure of clay.

Molecular dynamics (MD) modeling (Allen and Tildesley, 2017; Frenkel and Smit, 2001; Plimpton, 1995) is a viable tool for studying the mechanics and physics of clay at the nanoscale (e.g., Teich-McGoldrick et al., 2012; Bitzek et al., 2015; Song et al., 2018; Song and Wang, 2019; Song and Zhang, 2021; Zhang and Song, 2021, 2022, among others). Song et al. (2018) investigated the temperature

* Corresponding author.
E-mail address: xysong@ufl.edu (X. Song).

https://doi.org/10.1016/j.compgeo.2022.105037
Received 12 January 2022; Received in revised form 4 September 2022; Accepted 11 September 2022
Available online 1 October 2022

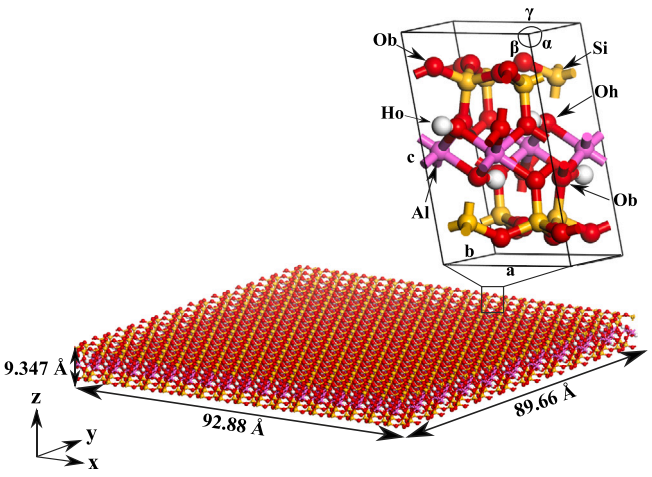

Fig. 1. MD model of the pyrophyllite sheet.

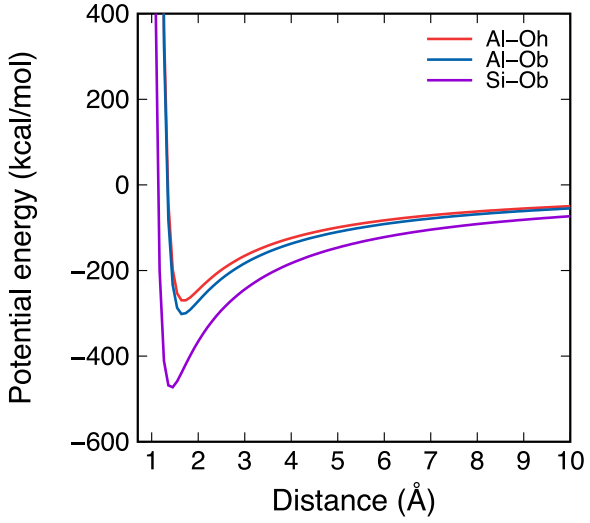

Fig. 2. Variations of potential energies with the distances of Al-Oh, Al-Ob, and Si-Ob.

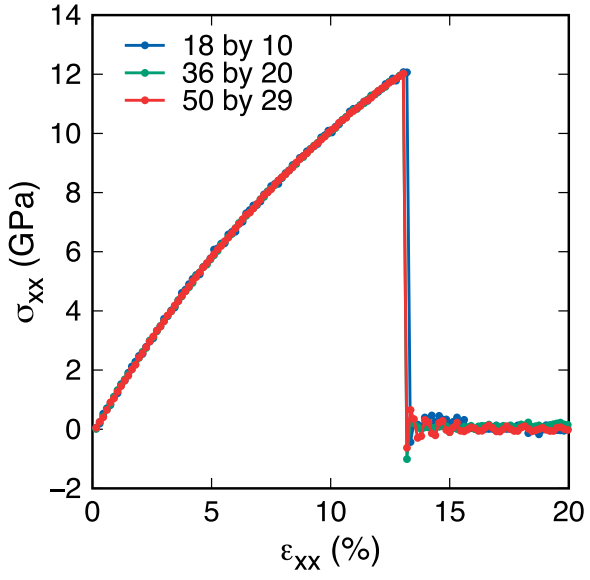

Fig. 3. Stress strain curves of the simulations under tensile loading with three clay sheet sizes.

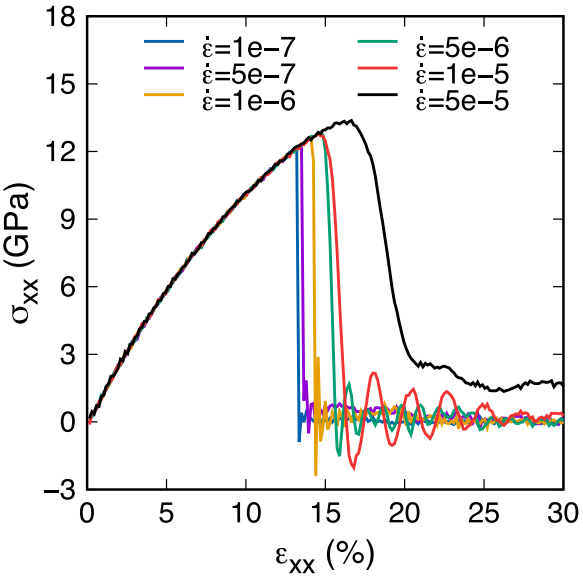

Fig. 4. Stress–strain curves under different tensile loading rates in the x-direction.

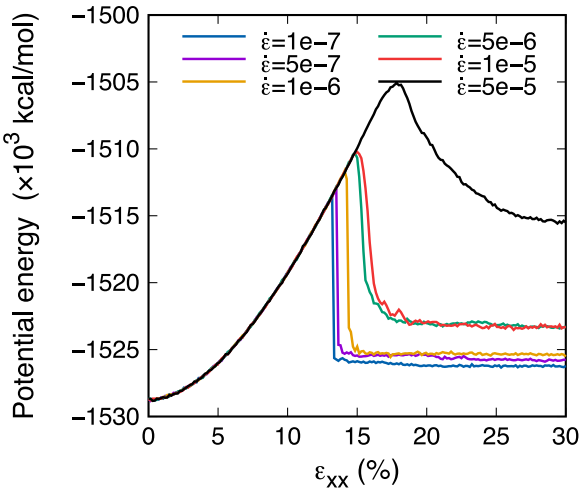

Fig. 5. Effect of strain rates on potential energy curves under tensile loading in the x-direction.

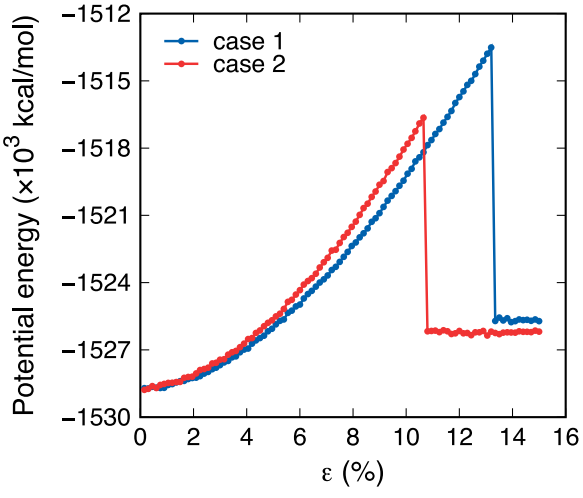

Fig. 6. Variations of potential energy under tensile loading in the x direction (case 1) and y direction (case 2), respectively. ($\dot{\epsilon} = 1 \times 10^{-7}$ fs^{-1}).

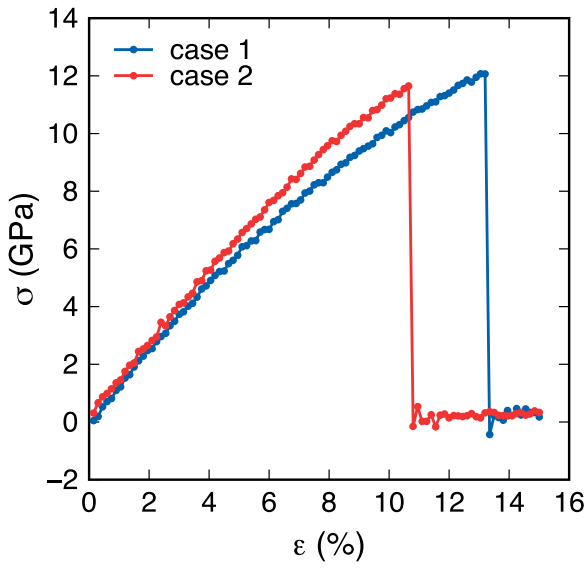

Fig. 7. Stress–strain curves under tensile loading in the x direction and y direction, respectively. ($\dot{\epsilon} = 1 \times 10^{-7}$ fs^{-1}).

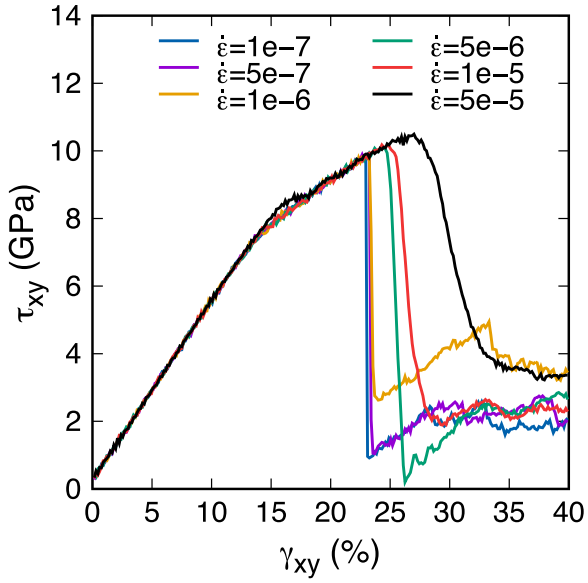

Fig. 8. Stress–strain curves for the simulations under shear loading at different strain rates.

dependence of capillary pressure and contact angle in unsaturated clay through MD modeling with the CHARMM force field (Vanommeslaeghe et al., 2010). Zhang and Song (2022) studied the nanoscale hydrodynamics of clay–water systems through nonequilibrium MD simulations with the ClayFF force field (Cygan et al., 2004). MD simulations have been used to study the elastic properties of clay (e.g., Zartman et al., 2010; Militzer et al., 2011; Ebrahimi et al., 2012; Teich-McGoldrick et al., 2012). Ebrahimi et al. (2012) studied the anisotropic elastic properties of Na-montmorillonite under water absorption using the original ClayFF force field (Cygan et al., 2004). Teich-McGoldrick et al. (2012) conducted the MD modeling with the ClayFF force field to study the elastic properties of muscovite and their dependence on temperature and pressure. MD has been applied to study the failure and cracking in clay under mechanical loading (e.g., Fu et al., 2011; Duque-Redondo et al., 2014; Hantal et al., 2014; Jia et al., 2021; Zhang et al., 2021). Hantal et al. (2014) studied the elastic and failure properties of clay with pre-existing cracks between clay sheets through MD with both the original ClayFF force field (Cygan et al., 2004) and ReaxFF force field (Van Duin et al., 2001). Their numerical results showed that the fracture toughness of layered clay from the MD simulations with ClayFF agrees well with experimental data. Jia et al. (2021) conducted an MD modeling of fracturing in kaolinite under high water pressure using ClayFF. We note that the study of cracking in clay using MD modeling has been focused on cracking between clay layers. However, the formation of in-plane cracks in an intact clay sheet has not been studied.

In this article, we investigate the formations of mode I and mode II cracks in an intact dry clay sheet under tension and shear respectively through MD modeling. The improved ClayFF force field (Pouvreau et al., 2019) that considers metal-O-H bending for stability is utilized in this study for the following reasons. First, the updated ClayFF is better than other force fields (e.g., ReaxFF) in modeling the elastic properties of clay. This feature is important for modeling crack formation in an intact clay sheet (i.e., no pre-existing crack) under mechanical loading. Second, the MD simulation in this study is a pure mechanical process without any chemical reaction. The formation of new chemical bonds is not required. We refer to Song et al. (2018) for a review of force fields for the MD modeling of clay. In this study, the notion of critical bond stretch is adopted to model the breakage of bonds between atoms in clay (see Section 3 for more discussions on this notion). The critical bond length for crack formation is determined by the radial distribution function and the force curve between a pair of atoms. The numerical results have shown that the mode I and II cracking in clay sheets is brittle and strain-rate dependent. We investigate the crack initiation under mode I and mode II loading conditions from the bond breakage analysis. We interpret the cracking mechanism in terms of the type and number of broken bonds in mode I and mode II cracking. We present the stress intensity factor and cracking energy release rate under both cracking modes. To validate our results, we compare the numerical results of the stress intensity factor and cracking energy release rate against the experimental and numerical data reported in the literature.

The remainder of this article is organized as follows. Section 2 introduces the molecular material model, the force field, and the numerical method. Section 3 presents the numerical results and discussions, followed by a closure.

2. Clay model and MD simulations

2.1. Clay model

The MD clay model consists of a dry pyrophyllite sheet in this work. The clay sheet is flawless with no pre-existing crack. Pyrophyllite is a standard 2:1 structure clay type with a tetrahedral–octahedral–tetrahedral (T–O–T) structure (Wardle and Brindley, 1972). Its chemical formula is $Al_2[Si_4O_{10}](OH)_2$. The 2:1 structure forms charge-neutral layers where tetrahedral and octahedral layers are composed of Si and Al. In this study we select pyrophyllite for the following reasons. First, pyrophyllite is a precursor to other clay minerals in the smectite group that provides mineral structures to these clays. Second, pyrophyllite has relatively high stability compared to other smectites such as montmorillonite which exhibits swelling upon water adsorption. Since there are no Si and Al vacancies or metal substitution in its structure, pyrophyllite requires no interlayer cations for charge compensation. Thus, the neutral charge of the clay sheets inhibits swelling when interacting with water. For these reasons, we simulate the pyrophyllite clay layer to investigate its crack mechanism under tensile and shear deformation. Fig. 1 shows the MD model of pyrophyllite. Atom types Ob, Si, and Al denote bridging oxygen, tetrahedral silicon, and octahedral aluminum. Ho and Oh are the interlayer hydroxyl hydrogen and hydroxyl oxygen forming the hydrogen bond. Lattice parameters of crystal pyrophyllite are a = 5.160 Å, b = 8.966 Å, and c = 9.347 Å. The crystal lattice is triclinic (non-orthogonal) with α = 91.18°, β = 100.46°, and γ =

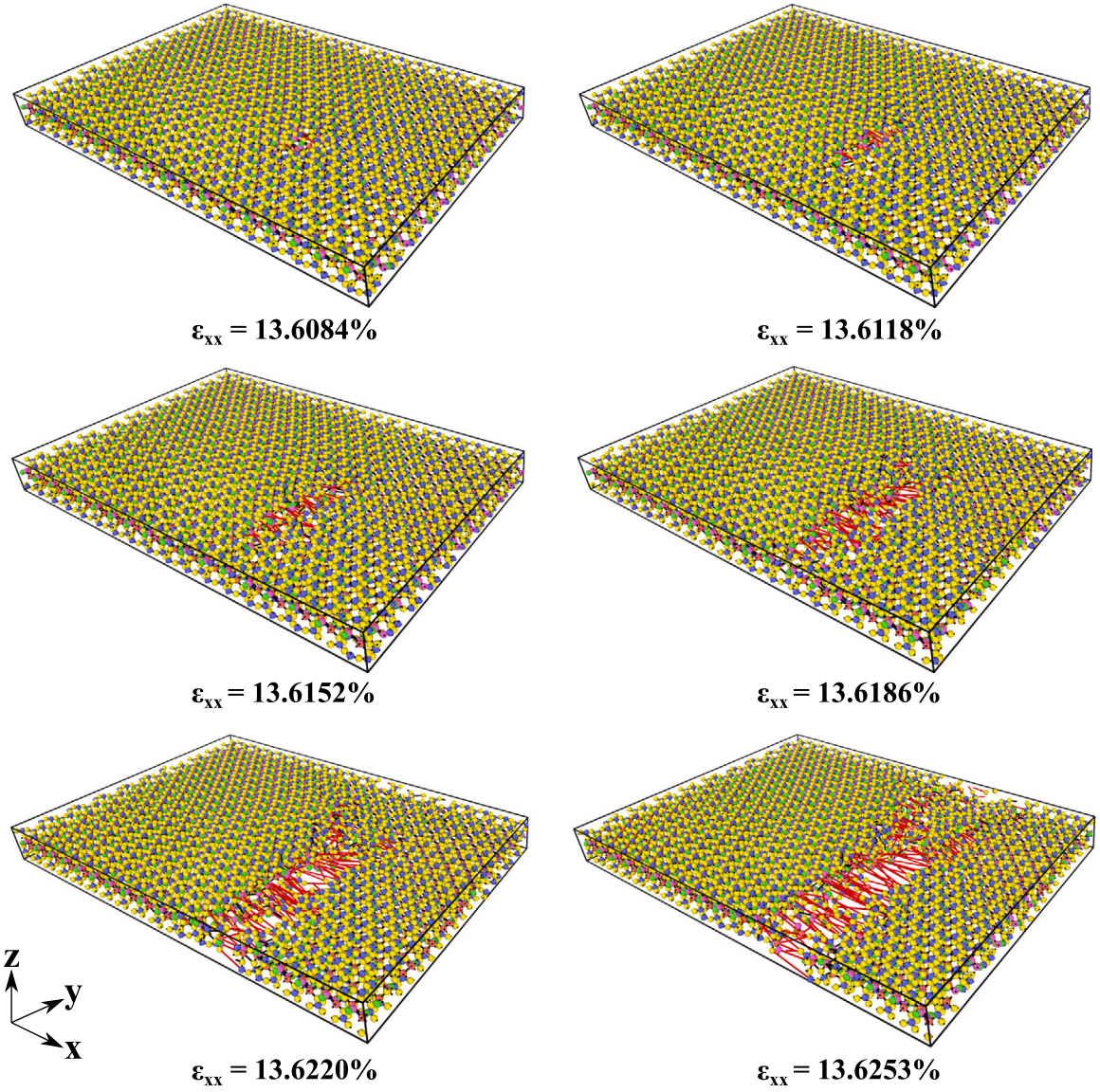

Fig. 9. Crack nucleation and propagation under tensile loading in the x direction with $\dot{\epsilon} = 1 \times 10^{-7}$ fs^{-1}.

89.64° (Lee and Guggenheim, 1981). The molecular model of the clay sheet is generated through replicating the unit cell of pyrophyllite by 18, 10, and 1 times in the a, b, and c dimensions, respectively. In this study, the initial dimensions of the pyrophyllite clay layer are 92.88 Å× 89.66 Å× 9.347 Å.

2.2. MD simulations

MD simulations are conducted on LAMMPS, a massively parallel molecular simulator (Plimpton, 1995). For the ClayFF force field, the total energy consists of nonbonded interactions (van der Waals and Coulombic energy) and bonded interactions (bond stretch and bend angle) (Cygan et al., 2004; Pouvreau et al., 2019). The van der Waals energy is represented by Lennard-Jones 12-6 function as

$$E_{vdw} = \sum_{i \neq j} D_{ij} \left[\left(\frac{R_{ij}}{r_{ij}} \right)^{12} - 2 \left(\frac{R_{ij}}{r_{ij}} \right)^{6} \right], \tag{1}$$

where r_{ij} is the distance between atoms i and j, D_{ij} and R_{ij} are respectively the depth of the potential well and the distance at which the interatomic potential energy vanishes. The Coulombic energy is written as

$$E_c = \frac{1}{4\pi\epsilon_0} \sum_{i \neq j} \frac{q_i q_j}{r_{ij}}, \tag{2}$$

where q_i and q_j are the atomic charges of atoms i and j, and ϵ_0 is the vacuum permittivity. The cutoff distance r_c is assumed 10 Å. Table 1 summarizes the values of non-bonded interaction parameters of the ClayFF force field for pyrophyllite. Fig. 2 plots the variation of the potential energies (the sum of energies related to van der Waals and Coulomb forces) between different atom pairs with their distances. The energies of the bond stretch term and the angle bend term are described by harmonic relationships as

$$E_b = k_1 (r_{ij} - r)^2, \tag{3}$$

$$E_a = k_2 (\theta_{ijk} - \theta)^2, \tag{4}$$

where k_1 and k_2 are force constants, r is the reference distance between two bonded atoms, θ_{ijk} is the rotational angle for the metal–oxygen–hydrogen, and θ is the reference angle. In this study, k_1 = 554.1349 kcal/mol Å^2, r =1 Å for O–H bond, k_2 = 15 kcal/mol rad^2, and θ= 110° for Al–O–H angle (Pouvreau et al., 2019).

The particle–particle particle-mesh method (Hockney and Eastwood, 2021) is used to compute the long-range Coulombic interactions.

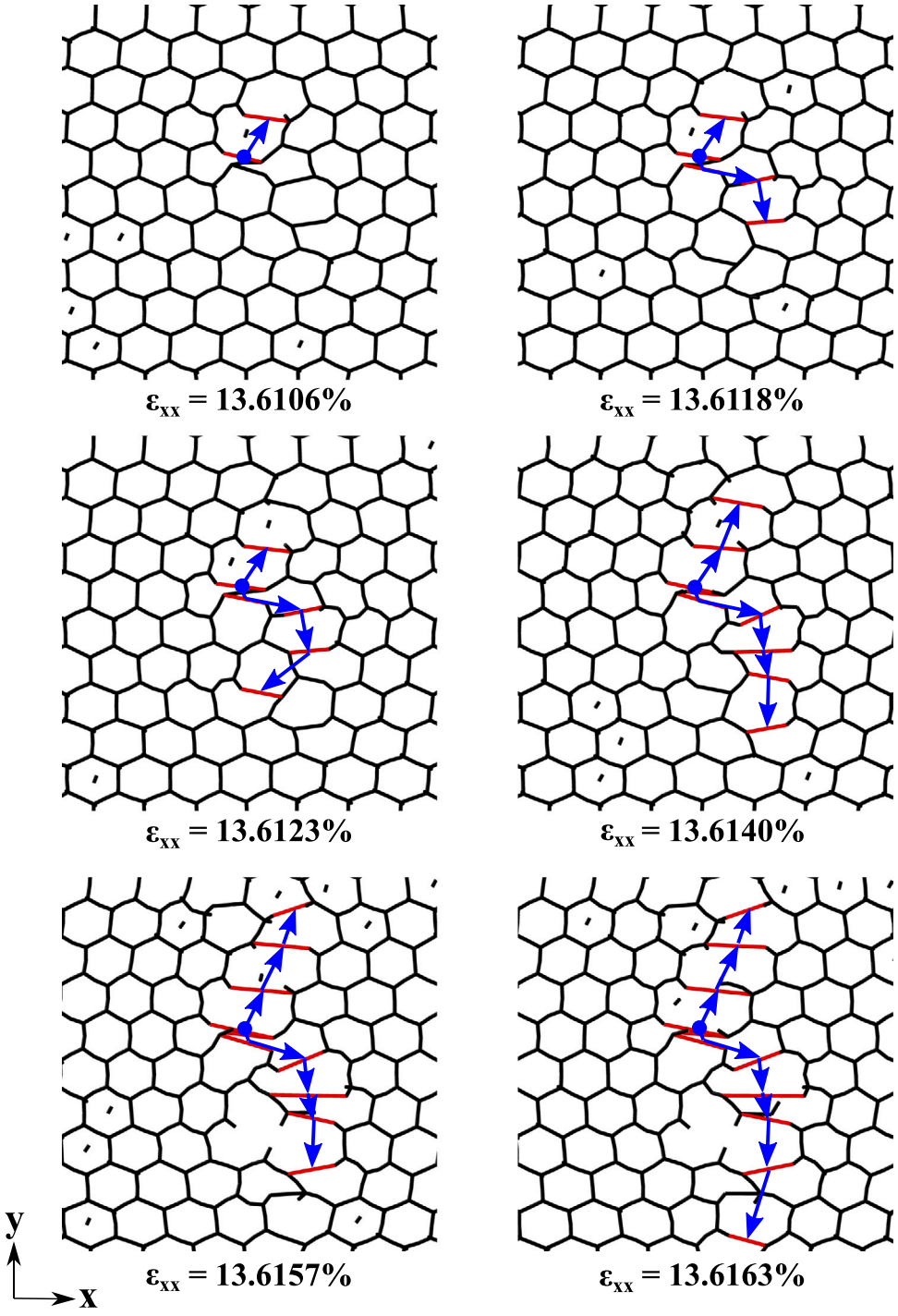

Fig. 10. Path of crack propagation in silicon layer under tensile loading in the x direction with $\dot{\epsilon} = 1 \times 10^{-7}$ fs^{-1}.

Table 1
Values of the nonbonded interaction parameters of the ClayFF force field (Cygan et al., 2004).

Atom type	Symbol	Charge (e)	D (kcal/mol)	R (Å)
Aluminum	Al	1.575	1.3298e−6	4.7963
Silicon	Si	2.1	1.8408e−6	3.7064
Bridging oxygen	Ob	−1.05	0.1554	3.5532
Hydroxyl oxygen	Oh	−0.95	0.1554	3.5532
Hydroxyl hydrogen	Ho	0.425	0	0

Periodic boundary conditions are applied in all directions. It allows particles to interact across the boundary and can exit one end of the box and re-enter the other end. Temperature and pressure are maintained using Nose–Hoover algorithm (Hoover, 1985). Note that the Nose–Hoover thermostat will not work well for arbitrary values of the damping parameter. The temperature damping parameter and pressure damping parameter should be of around 100 time steps and 1000 time steps, respectively (Plimpton, 1995). For this work, the time step is 1 fs (i.e., 10^{-15} s). Thus, the damping parameters are 100 fs and 1000 fs for temperature and pressure, respectively.

The Verlet velocity algorithm is employed to integrate the equations of motion of atoms. We employ the isobaric–isothermal NPT ensemble

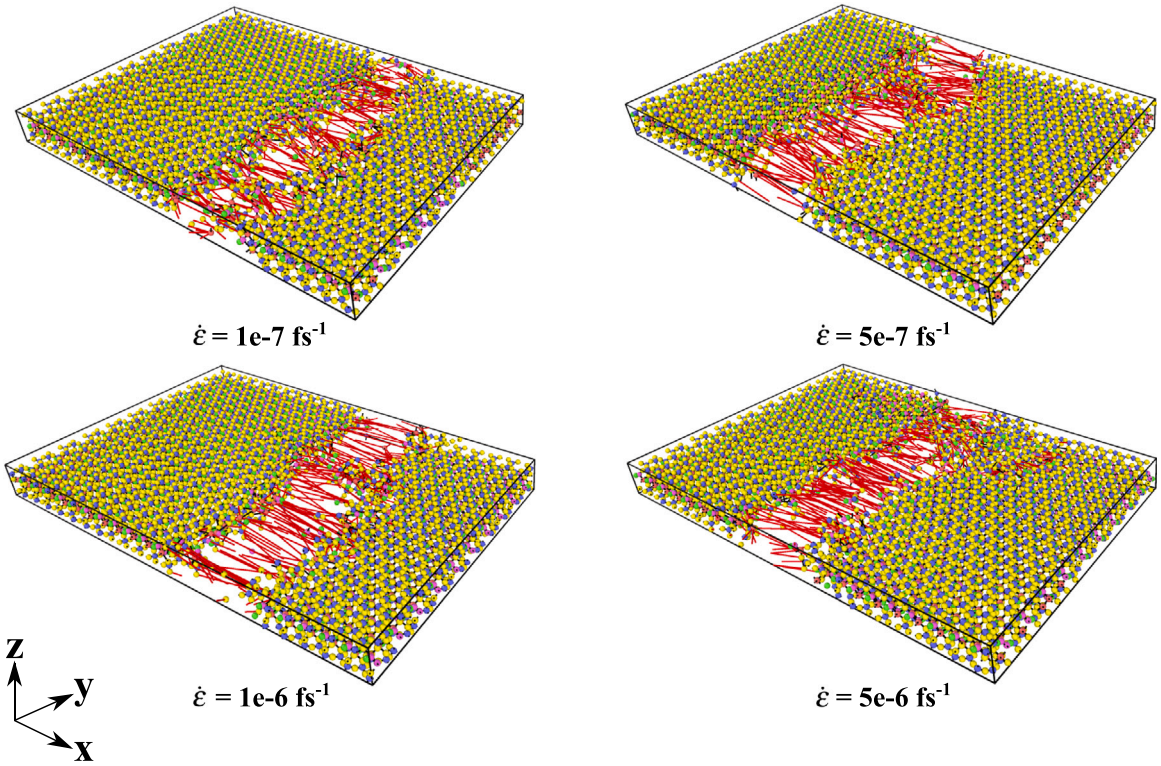

Fig. 11. Comparison of crack patterns between different strain rates at strain ϵ_{xx} = 22.5%.

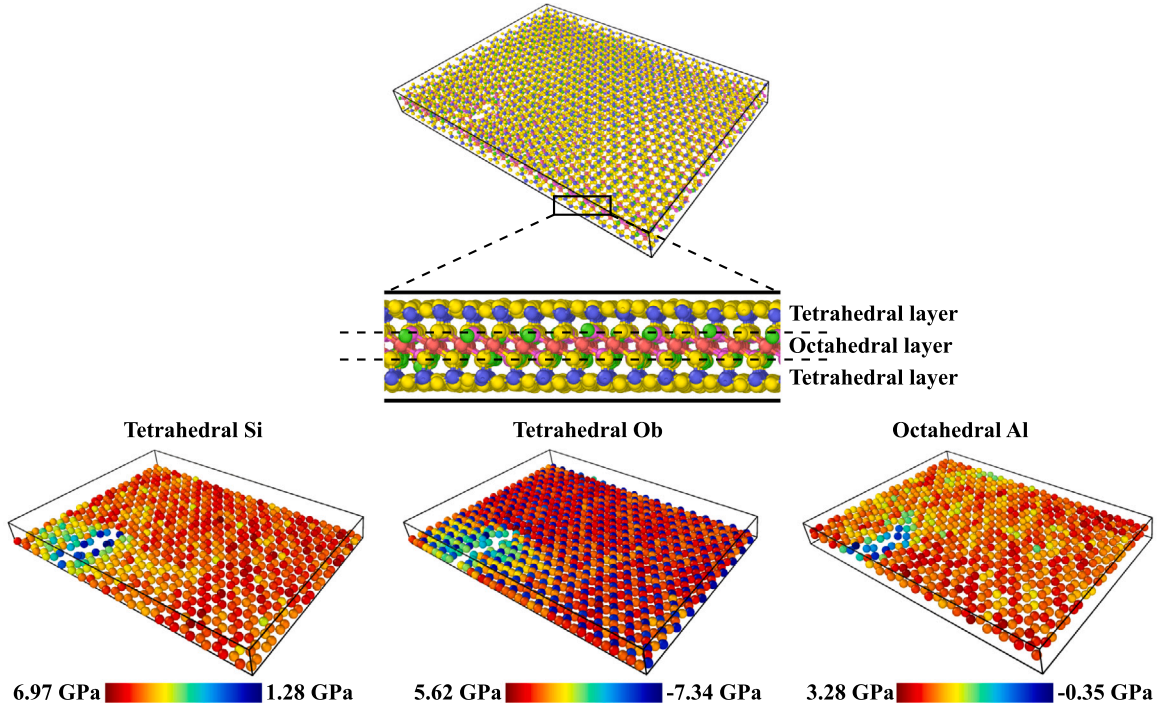

Fig. 12. Contour of σ_{xx} in the tetrahedral silicon layer, tetrahedral bridging oxygen layer, and octahedral aluminum layer at ϵ_{xx} = 13.35%. ($\dot{\epsilon}$=1e-7 fs^{-1}).

(constant number of atoms, constant pressure, and constant temperature) to equilibrate the atomic positions and volume at 298 K for 6 ns with a barostat coupling constant of 1000 fs. We couple the system to zero external pressure and allow the system to change the volume but not the shape. The equilibrium state is verified by the convergence of potential energy and system pressure. Our preliminary study shows that the system has reached a steady state after 6 ns during the equilibrium stage. The equilibrated system serves as the starting point for applying tensile or shear deformation. Since MD modeling is computationally expensive, all simulations are conducted with 128 CPU cores on a supercomputer. The wall clock time for the simulation of 6 ns for the system to reach equilibrium is about 6 h. The run time for production under a tensile strain of 0.3 is around 3 h.

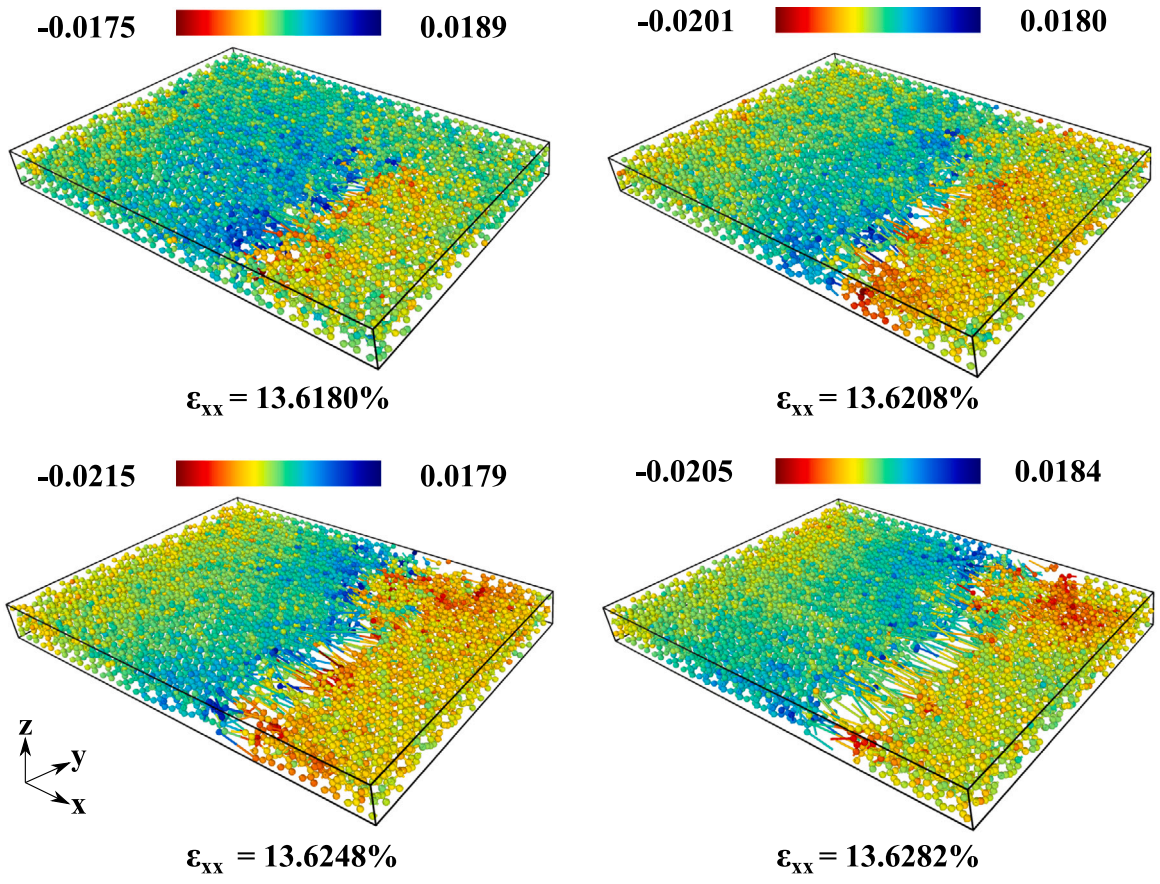

Fig. 13. Contour of atomic velocity v_x under tensile loading in the x direction with $\dot{\epsilon} = 1 \times 10^{-7}$ fs^{-1}. Velocity unit: Å/fs.

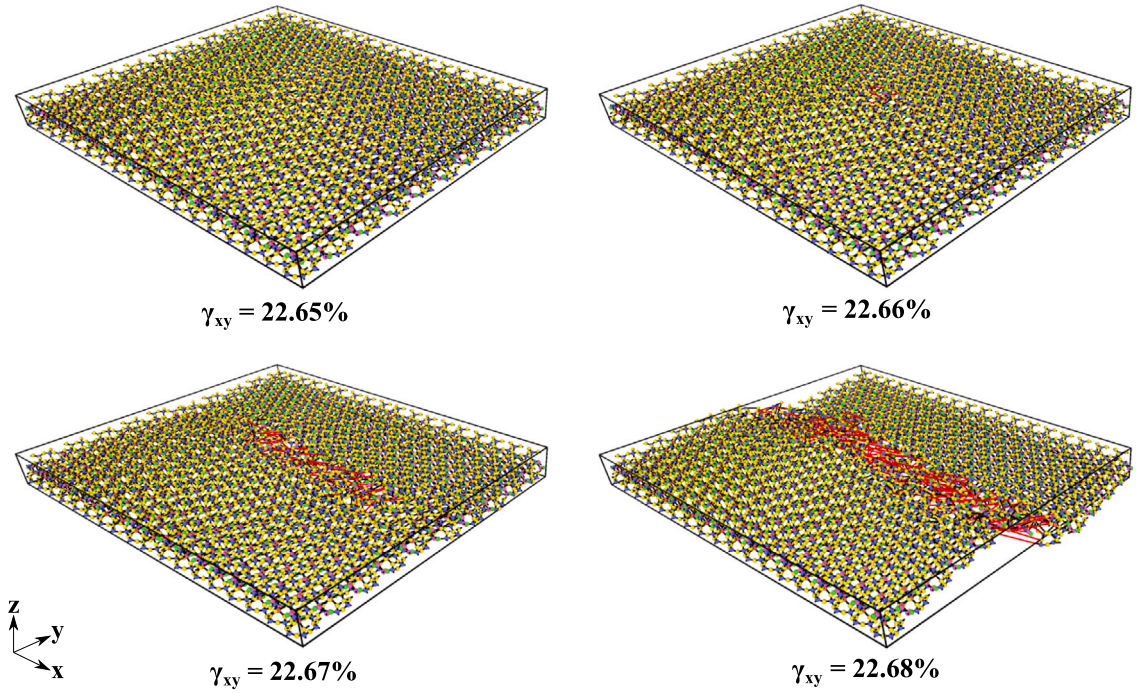

Fig. 14. Snapshots of crack formation under shear loading (Crack zone in red) with $\dot{\epsilon} = 1 \times 10^{-7}$ fs^{-1}.

It is more convenient to control strain than stress in MD simulations. Thus, in this study the strain conrolled method is adtopted. After the relaxation of the initial system, uniaxial tensile deformation is applied to the equilibrated clay particle by the strain-controlled loading method. The periodic simulation box is deformed at a constant engineering strain rate along a specified direction in this approach. At

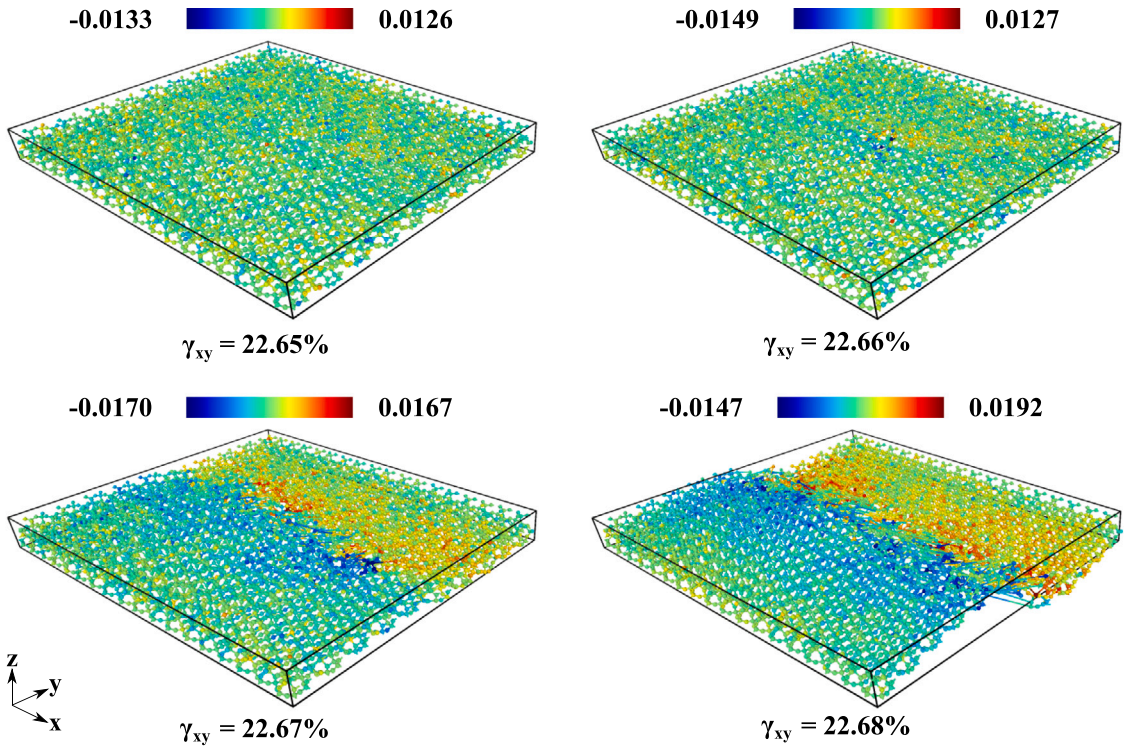

Fig. 15. Contour of atomic velocity v_x under shear loading with $\dot{\epsilon} = 1 \times 10^{-7}$ fs^{-1}. Velocity unit: Å/fs.

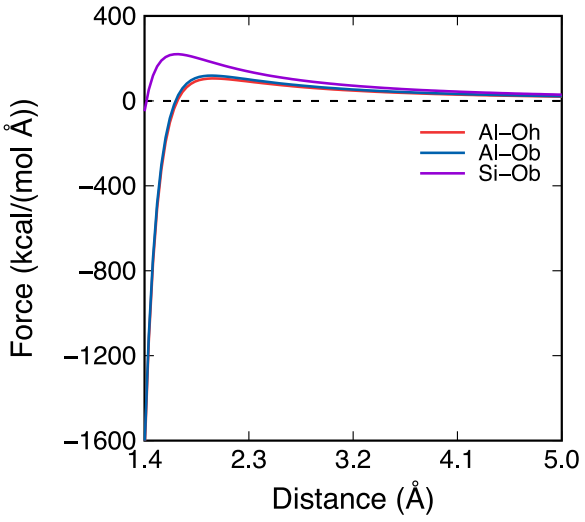

Fig. 16. Variations of bonds forces with the distance between atom pairs.

each time step when the dimension of the simulation box is changed, we remap atomic positions following the migration of the simulation box boundaries. The remap operation forces the atoms to deform via an affine transformation that exactly matches the deformation of the simulation box, which is appropriate for MD simulations of solids (Plimpton, 1995). In the strain-controlled loading method, tensile strain is the ratio of the length change to the original box length. As we deform the simulation box at a constant engineering strain rate, pressure components in the x, y, and z directions are controlled independently to allow transverse deformations due to the Poisson effect. For example, as the simulation volume is deformed along the x direction, we apply the free transverse pressure condition by assigning zero pressure to the y and z directions of the system. The stress tensor is computed globally for all atoms in the system. The molecular visualization tool of OVITO (Stukowski, 2009) is used to visualize and analyze the simulation data in this study.

3. Numerical results

This section analyzes the fundamental mechanism of cracking in dry clay sheets from MD simulations. First, we present the stress strain curves under tensile and shear loading at different loading rates. For the case under tensile loading we run simulations under loading in the x and y directions respectively to show the anisotropic behavior of clay sheets. Here x and y correspond to the a-axis and b-axis respectively as plotted in Fig. 1. Second, we analyze the formation of cracks from the snapshots of the deformed configurations under tensile and shear loading conditions. Third, the critical bond lengths between atom pairs are determined by the force curve (maximum value) and radial distribution function (minimum value). We further analyze the mechanism of crack formation in clay sheets using the notion of a critical bond stretch in terms of the number and percentage of broken bonds. Fourth, we compute the stress intensity factor and energy release rate during crack formation. Our preliminary numerical results demonstrate that the numerical results are insensitive to the clay sheet sizes used in this study. Fig. 3 shows the stress–strain curves from the simulations with three clay sheet sizes which consist of 18 ×10, 36× 20, and 50 × 29 unit cells in the x–y plane, respectively. The results in Fig. 3 show that the stress–strain curve is independent of clay sheet sizes. Thus, for all numerical simulations we adopt the clay sheet size that consists of 18 × 10 unit cells in the x–y plane for computational efficiency.

3.1. Stress–strain curves under tension and shear at different loading rates

In this study, we adopt the virial stress tensor to describe the stress state in the clay sheet. Virial stress was developed based on the virial theorem (Clausius, 1870; Maxwell, 1870). It was originally proposed to determine the stress field applied to the surface of a system containing atomic interactions (Zimmerman et al., 2004). Subramaniyan and Sun (2008) demonstrated the equivalence of the atomic–scale virial stress

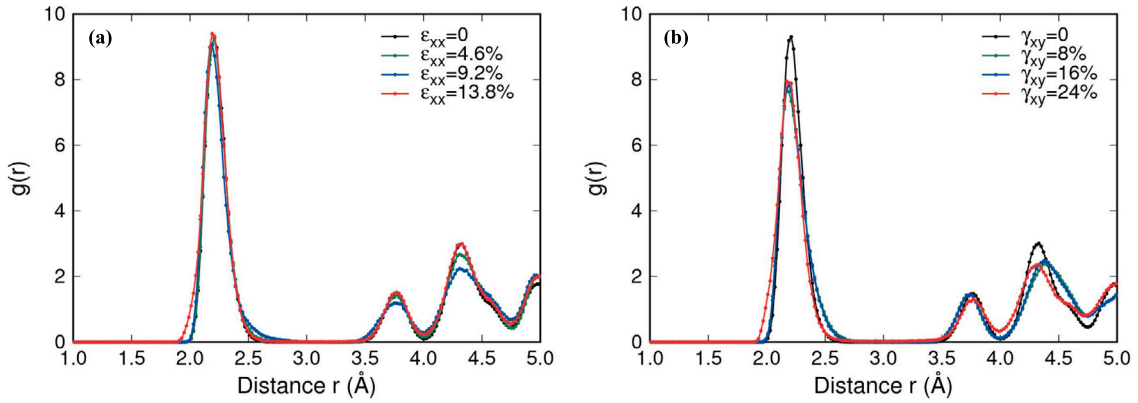

Fig. 17. Radial distribution function for Al-Ob under (a) tensile and (b) shear deformation.

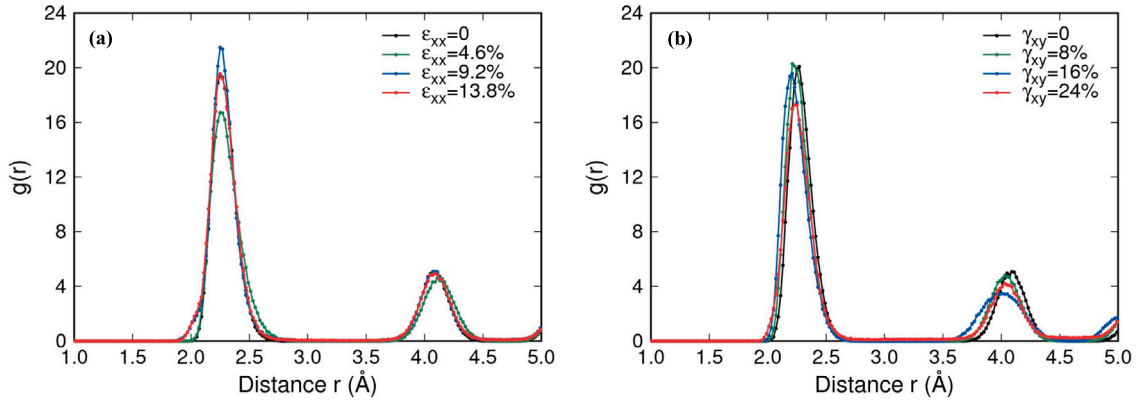

Fig. 18. Radial distribution function for Al-Oh under (a) tensile and (b) shear deformation.

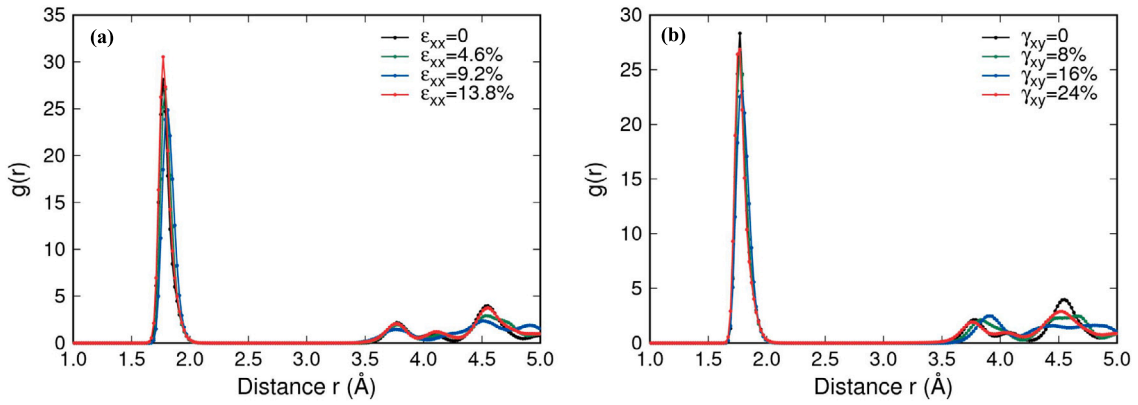

Fig. 19. Radial distribution function for Si-Ob under (a) tensile and (b) shear deformation.

and continuum–scale Cauchy stress. Note that virial stress tensor could account for temperature effect by incorporating the contribution from kinetic energy. The virial stress tensor can be written as

$$\sigma_{ij} = \frac{1}{V}\sum_{A=1}^{N}\left[\frac{1}{2}\sum_{B=1}^{N_c}\left(r_i^B - r_i^A\right)F_j^{AB} - m^A v_i^A v_j^A\right], \tag{5}$$

where V is the total volume of the atomistic system, N is the total number of atoms in the system, i and j = x,y,z (i.e., x–y–z directions), N_c is the number of neighboring atoms of atom A within a cutoff radius r_c, r_i^A and r_i^B are the positions of atoms A and B along the direction i, F_j^{AB} is the force exerted by atom B on atom A, and m^A and v^A denote the mass and velocity of atom A, respectively.

Fig. 4 shows the impact of strain rates on the stress–strain curves of pyrophyllite under uniaxial tension in the x direction. The linear elastic regime corresponds to the range of strain from zero to 5%. The nonlinear stage takes place as the tensile strain exceeds 5% and strain hardening can be observed. Brittle fracture happens as the stress–strain curves abruptly drop to zero from the peak stress. Fig. 5 plots the variations of potential energy for the simulations with different loading rates. The strains where the potential energy curves drop after the peak may imply the failure of clay sheets with crack propagation. Comparison of the results in Figs. 4 and 5 shows that the peak values of the stress and potential energy are consistently at the same strain for each simulation. Thus, in this study the peak stress of the stress–strain curve is assumed as the failure strength of the clay sheet. The results in Fig. 4 show that the ultimate tensile strength exhibits the strain rate

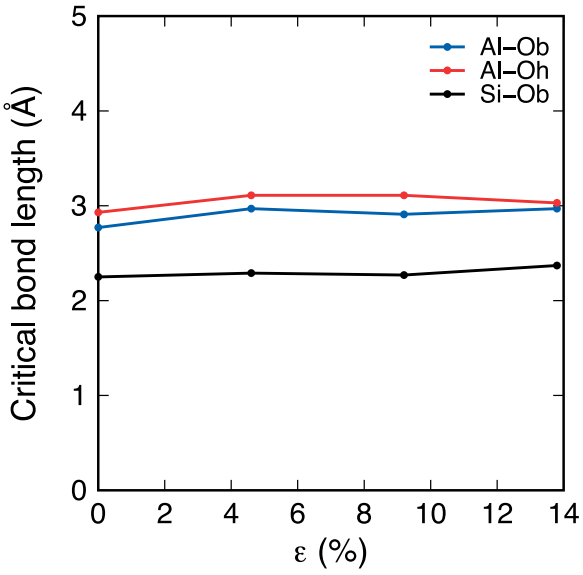

Fig. 20. Critical bond lengths of different types of atom pairs.

dependence. It increases as strain rates increase. For the case of the maximum strain rate tested in this study, $\dot{\epsilon} = 5\times10^{-5}$ fs^{-1}, the ultimate tensile strength reaches 13.4 GPa at the strain around 16.7% while the minimum strain rate ($\dot{\epsilon} = 1\times10^{-7}$ fs^{-1}) gives an ultimate strength of 12.2 GPa at the strain around 13.2%. Tensile stress begins to drop after the peak value as crack propagates. Once the tensile stress reaches zero, it starts to oscillate due to a spring-back phenomenon (Zhou et al., 2008). The strain rate less than 5×10^{-7} fs^{-1} has little effect on the stress–strain curve.

Two loading scenarios are simulated to investigate the impact of the atomic structural anisotropy on the mechanical properties of clay under tensile loading. Tensile loads are applied in the x direction for case 1 and in the y direction for case 2. Figs. 6 and 7 compare the potential energy and stress–strain curves for the two cases at the strain rate 1×10^{-7}fs^{-1}. The failure happens earlier for the case under tensile loading in the y direction (10.7%) than that in the x direction (13.3%). The ultimate tensile strengths are 12.1 GPa and 11.6 GPa for the cases of tensile loading in the x direction and y direction, respectively. This finding indicates that pyrophyllite has a greater stiffness in the x direction than in the y direction, which is consistent with the result in the literature (Teich-McGoldrick et al., 2012). The potential energy curve shows a higher peak value of −1513508 kcal/mol for the case under the tensile loading in the x direction and a larger energy release upon cracking. By comparison, the peak value of potential energy for the case under tensile loading in the y direction is −1516639 kcal/mol.

Fig. 8 presents the stress strain curves for the simulations under shear loading at different loading rates ranging from 1×10^{-7} fs^{-1} to 5×10^{-5} fs^{-1}. The linear elastic regime ends at the shear strain around 15%. The peak shear stress decreases as the strain rate decreases. It can be found that the strain rates less than 5×10^{-7} fs^{-1} gives almost identical shear stress–strain curves. The strain-rate dependence behavior is similar to that in tensile loading. Thus, in what follows we present the numerical results of simulations performed at the strain rate 1×10^{-7}fs^{-1} except for comparison purpose in which the results at other strain rates will be provided. Next, we analyze the dynamics of crack formation under tensile and shear loading, respectively.

3.2. Crack nucleation and propagation

We study the dynamics of crack formations in the clay sheet from its deformed configurations under tensile and shear loading conditions, respectively. In this study, it is hypothesized that the bond between two atoms breaks when the distance between them is greater than a critical value, called the critical bond length (see Section 3.3 for determination of critical bond lengths in this study). The crack naturally forms in the clay sheet if enough bonds (i.e., atomic interactions) are broken. Fig. 9 shows the formation of crack in the clay sheet under tensile loading in the x direction with $\dot{\epsilon} = 1\times10^{-7}$ fs^{-1}. Crack generally develops perpendicular to the direction of the applied tensile load. Crack occurs first near the middle of the clay particle, and propagates in both directions of the y axis. The increase in tensile strain from crack nucleation to full propagation is about 0.02%, which may imply that the failure mode of the clay sheet is brittle.

Fig. 10 presents the path of crack propagation in the tetrahedral silicon layer under tensile loading in the x direction with $\dot{\epsilon} = 1\times10^{-7}$ fs^{-1}. The blue dot denotes the location where crack initializes. The path of crack propagation is tracked based on the position of broken bonds which are in red. It shows that the crack propagation direction is not strictly perpendicular to the loading direction but with an angle. This could be attributed to the hexagon structure of the silicon layer. Fig. 11 compares crack patterns at different strain rates ranging from 1×10^{-7} fs^{-1} to 5×10^{-6} fs^{-1}. Bonds longer than the critical bond length are highlighted in red. The determination of the critical bond length for bond breakage is discussed in the following section. As the strain rate reaches 5×10^{-6} fs^{-1}, the crack pattern switches from a single fracture to multiple slippages of rows of atoms. Our numerical results show that a strain rate less than 1×10^{-6} fs^{-1} could be sufficiently small to prevent the occurrence of multiple cracks.

Next, we analyze the contour of stress in the clay sheet. The local stress tensor for an atom can be written as

$$\sigma_{ij} = \frac{1}{V_a}\left(-mv_iv_j - W_{ij}\right), \tag{6}$$

where mv_iv_j is the kinetic energy, W_{ij} is the virial contribution due to inter-atomic interactions, including pairwise energy, bond term and angle term energy, and the K-Space contribution from long-range Coulombic interactions (Plimpton, 1995), V_a is the atomic volume estimated by Voronoi method (Rycroft, 2009). Due to the layered inhomogeneity, we divide the T–O–T clay structure into sublayers with the same atom type, e.g., aluminum sublayer, silicon sublayer, and bridging oxygen sublayer, as shown in Fig. 12. Then we characterize atomic stress in these individual layers. Fig. 12 presents the contours of atomic tensile stress σ_{xx} for tetrahedral silicon layer, surface bridging oxygen layer, and octahedral aluminum layer. One observation is that the atoms near the crack edge have minimum stress. For example, in the silicon sublayer and aluminum sublayer, the minimum σ_{xx} occurs near the crack. It is also found that the atomic stress generally increases with the increasing distance from the crack edge.

Fig. 13 presents the contours of the atomic velocity v_x at four loading stages under tensile loading in the x direction. The atoms on the left and right sides of the crack surface move in opposite directions at a similar speed. The results show little changes in velocity as the crack propagates. For example, the atomic velocity varies between 0.0179 Å/fs and 0.0189 Å/fs for the atoms moving along the positive direction of the x axis. This observation agrees with the strain-controlled loading approach. That is, atom velocities are uniform due to the uniform stretch rate of the simulation box.

Finally, we present the results of the crack formation under shear loading. In this case, shear deformation is applied at a constant rate by shearing the simulation boundary box with a constant system volume. As shown in Fig. 8, the ultimate shear stress 9.8 GPa is obtained at the strain 22.6%, followed by the sharp decrease signifying the crack nucleation in the clay sheet. Fig. 14 presents the snapshots of the clay sheet during crack propagation under shear loading with $\dot{\epsilon} = 1\times10^{-7}$ fs^{-1}. Bond breaking occurs near the center of the clay sheet and crack propagates horizontally as expected. Fig. 15 plots the contours of atomic velocity v_x at different shear strains in the mode II cracking process. Next, we determine the critical bond length through radial distribution functions and force curves between atom pairs.

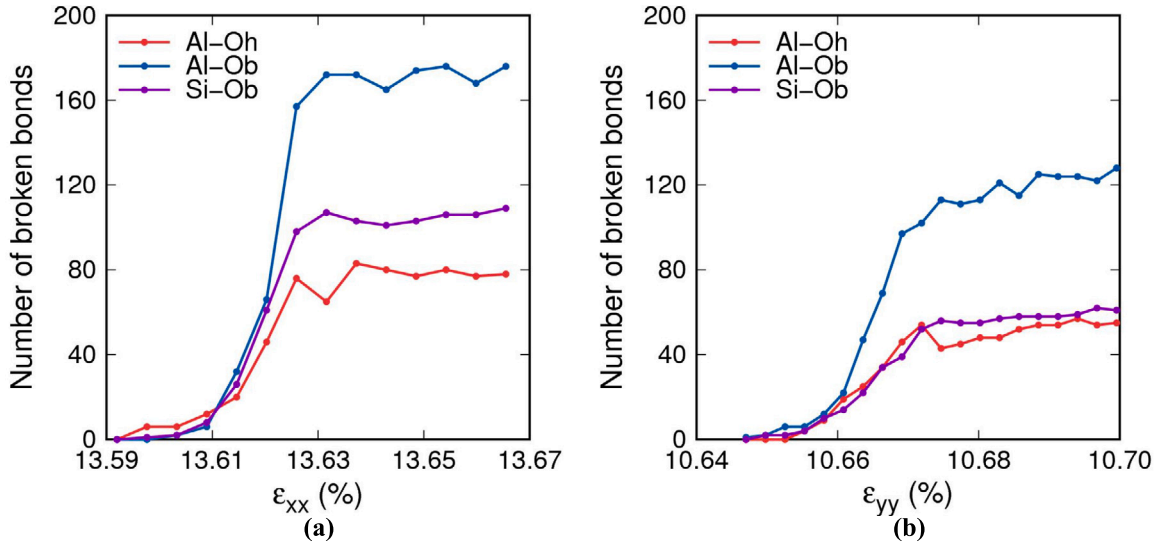

Fig. 21. Number of broken bonds under tensile loading (mode I crack).

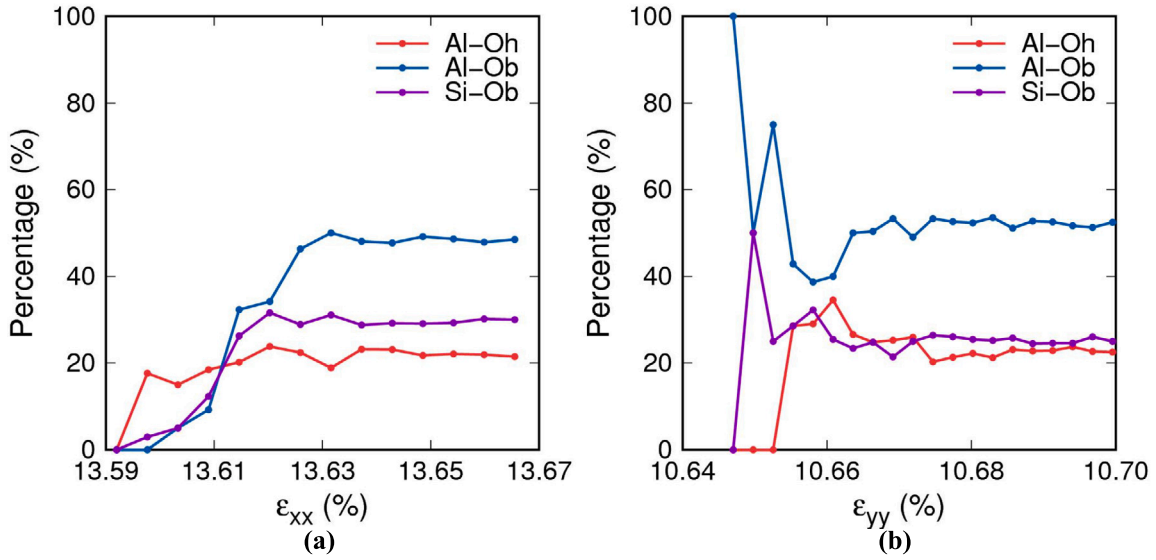

Fig. 22. Percentage of broken bonds under tensile loading (mode I crack).

3.3. Critical bond length

In this study, we apply the notion of critical bond stretch to study the bond breakage mechanism in the process of cracking. We determine the critical bond length through force curves and radial distribution functions between atom pairs. Fig. 16 plots the atomic force between atom pairs as a function of their distance. Here the atomic force is a quantity describing the repulsion or attraction between an atom pair. As the distance reaches 5 Å, atomic forces between atom pairs Al-Oh, Al-Ob, and Si-Ob are close to zero. From this observation, we may assume that the maximum critical bond length for each atom pair is 5 Å. This is a rough approximation without considering the deformation of the clay sheet (i.e., individual bond breakage under deformation). Therefore, we apply radial distribution functions during the deformation with cracking to determine the minimum critical bond length for each atom pair.

In statistical mechanics, the radial distribution function (RDF, also called pair correlation function) of a system of particles describes how density varies as a function of distance from a reference particle. RDF is a measure of the probability of finding a particle at a distance r away from a given reference particle. The general algorithm involves determining the number of particles within a distance between r and $r + dr$ away from a particle. RDF is usually determined by calculating the distance between particle pairs and binning them into a histogram. The histogram is then normalized with respect to an ideal gas, where particle histograms are completely uncorrelated. For the clay sheet in our MD simulation, this normalization is the number density of the system ρ multiplied by the volume of the spherical shell, $\rho 4\pi r^2 dr$. Thus, given the number of atoms $dn(r)$ at a distance between r and $r+dr$ from a reference atom, the radial distribution function $g(r)$ can be written as

$$g(r) = \frac{dn(r)}{\rho 4\pi r^2 dr}. \tag{7}$$

By computing RDFs of different atom pairs, we can obtain critical bond lengths for different bonds, e.g., Al-Ob, Al-Oh, and Si-Ob. Fig. 17, 18 and 19 plot RDFs for three atom pairs, Al-Ob, Al-Oh, and Si-Ob, under tensile and shear deformation, respectively.

In coordination chemistry, the first coordination sphere refers to the array of atoms directly attached to the reference atom. Since the first minimum after the first peak in $g(r)$ can be considered as the radius of

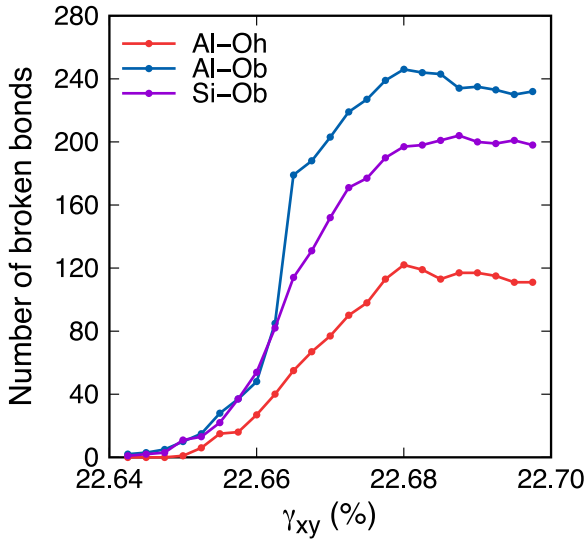

Fig. 23. Number of broken bonds under shear loading (mode II crack).

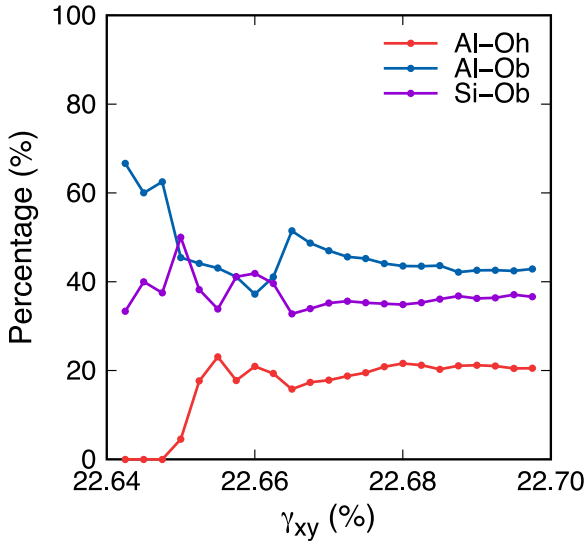

Fig. 24. Percentage of broken bonds under shear loading (mode II crack).

the first coordination sphere (Gereben and Petkov, 2013; Yang et al., 2017), we can assume the radius as the critical bond length above which the atom pair is broken. Fig. 20 plots the variations of critical bond length with strain for different atom pairs. We then determine the minimum critical bond lengths for Al-Ob, Al-Oh, and Si-Ob, which are 2.91 Å, 3.05 Å, and 2.30 Å, respectively. Next, we analyze the bond breakage in the cracking process using the minimum critical bond lengths for the three atom pairs.

3.3.1. Number and percentage of broken bonds

Based on the critical bond length computed from radial distribution functions, we compute the number and percentage of broken bonds for the three types of atom pairs during the cracking process under tensile and shear loading conditions. The results of model I cracking are shown in Figs. 21 and 22. The results in Figs. 21 and 22 show that in all broken bonds, Al-Ob bonds account for the largest percentage, followed by Si-Ob and Al-Oh bonds.

In the two tensile loading cases, the number of broken bonds first increases with crack nucleation and growth, and finally reaches a steady state indicating a fully developed crack. The analysis of broken bonds

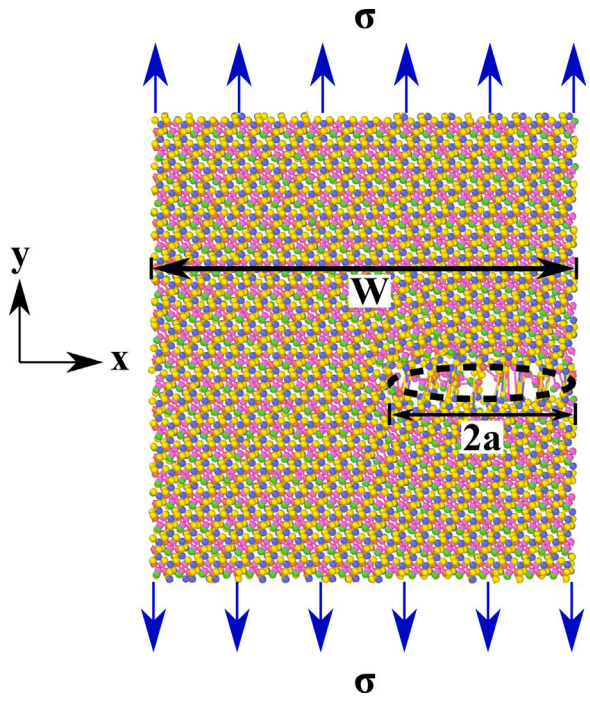

Fig. 25. Schematics of the mode I crack and the geometrical parameters for the stress intensity factor.

may help to understand the effect of molecular structural anisotropy on crack formation in the pyrophyllite sheet at the atomic scale. As shown in Fig. 7, the ultimate tensile strength in the x direction is greater than that in the y direction. This is consistent with the broken bonds profiles. According to Fig. 21, the average number of total broken bonds is 358 under tensile loading in the x direction and this number is 240 for tensile loading in the y-direction. In addition, the strain corresponding to the maximum number of broken bonds under tensile loading in the y direction is 10.69%. This number is much smaller than that for the case of tensile loading in the x direction, which is 13.63%.

The percentage is defined as the ratio of the number of one type of broken bonds to the total number of broken bonds. A bond starts to break in the Si-Ob layer at the tensile strains of 13.598% and 10.65%, respectively, for the simulations under tensile loading in the x and y directions. For both cases, Al-Ob bonds occupy the largest percentage of broken bonds, followed by Si-Ob and Al-Oh bonds. For the tensile loading in the x direction, the final percentages of Al-Oh, Al-Ob, and Si-Ob broken bonds at the end of cracking are approximately 21.5%, 53.2%, and 24.5%, respectively. Similarly, for the tensile loading in the y direction the final percentages of Al-Oh, Al-Ob, and Si-Ob broken bonds are approximately 22.4%, 53.2%, and 24.5%, respectively. For both cases, no broken bonds are found in hydrogen bonds.

For the mode II cracking under shear loading, the results are presented in Figs. 23 and 24. The percentages of Al-Oh, Al-Ob, and Si-Ob broken bonds are 20.5%, 42.9%, and 36.6%, respectively. The bond breakage behavior is consistent with that in mode I cracking.

3.4. Stress intensity factor

In continuum fracture mechanics, the resistance of a material to crack propagation can be characterized by stress intensity factor (Anderson, 2017). For mode I cracking, the stress intensity factor reads

$$K_I = \sigma\sqrt{\pi a}\left[\frac{W}{\pi a}\tan\left(\frac{\pi a}{W}\right)\right]^{1/2}, \tag{8}$$

where σ is the tensile stress, a is one half of crack length, W is the width of the clay sheet. In this study, $W = L_x$ when tensile loading

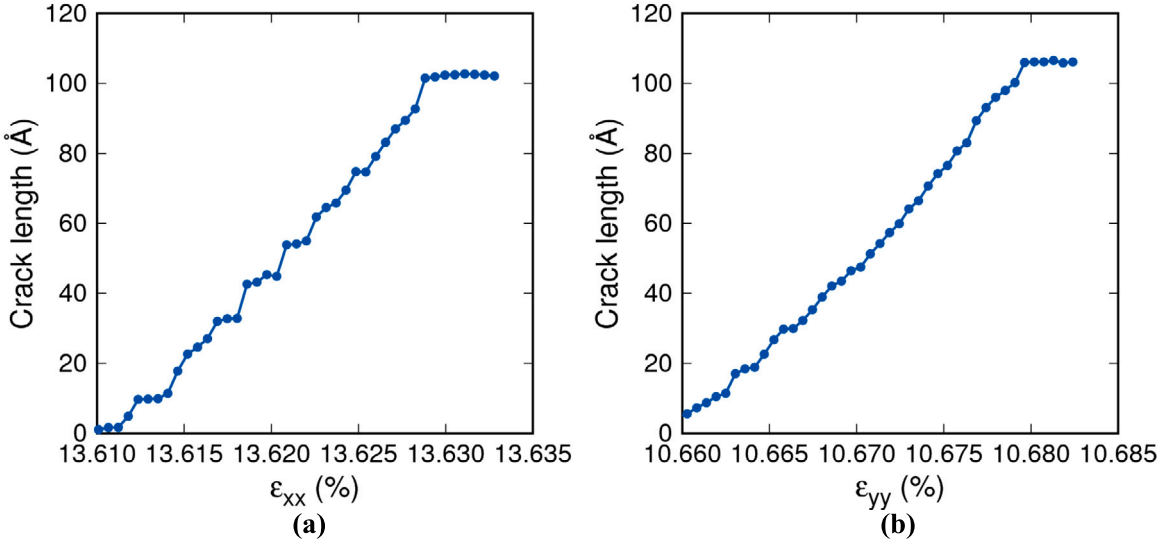

Fig. 26. Crack length during crack propagation under tensile loading (mode I crack) in (a) x-direction and (b) y-direction at $\dot{\epsilon} = 1 \times 10^{-7}$ fs^{-1}.

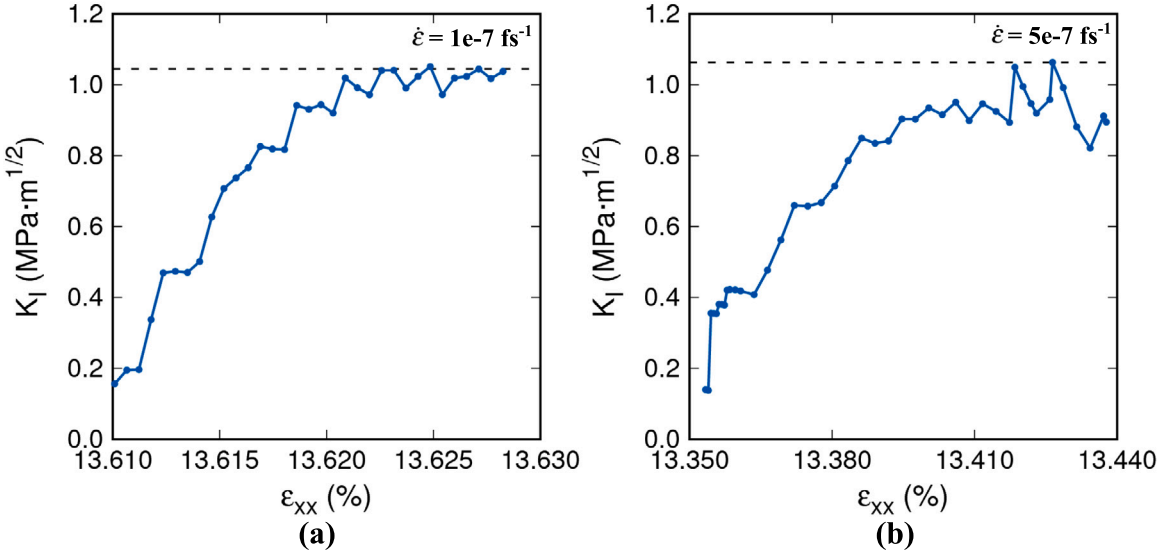

Fig. 27. Stress intensity factor of clay under tensile loading (mode I crack) in x-direction at strain rates (a) 1×10^{-7} fs^{-1} and (b) 5×10^{-7} fs^{-1}.

is applied in the y-direction. We note that Eq. (8) applies for colinear cracks. Fig. 25 schematically illustrates the configuration for computing the mode 1 stress intensity factor K_I under tensile loading along the y direction. Note that the closed-form solution (e.g.,. Eq. (8)) for stress intensity factor was derived for continuum fracture mechanics. However, a few studies have successfully applied the closed-form solution to obtain K_I from MD simulations (Le and Batra, 2016; Han et al., 2017). In this study, we determine K_I using Eq. 28 for the mode I crack in clay sheets. The crack length is measured by the distance between two outermost broken bonds. Trajectories of atoms are output directly from MD simulations during crack propagation. Fig. 26 plots the variation of crack length during crack propagation under tensile loading. The results of the simulations under tensile loads in the x direction and y direction respectively show approximately linear increase in crack length with respect to tensile strain. When the tensile strain reaches $\varepsilon_{xx} = 13.63\%$ or $\varepsilon_{yy} = 10.68\%$, the clay sample is completely fractured as indicated by a constant crack length. In general, for mode I crack a critical value is referred to as the critical stress intensity factor, or fracture toughness of the material. That is, the stress intensity factor must exceed this critical value for the crack to propagate in samples with a pre-existing crack. However, in this study no pre-crack exists in the clay sample before loading. Alternatively, we compute the maximum stress intensity factor for different loading conditions to compare the resistance to crack propagation. Fig. 27 compares the variations of stress intensity factor during crack propagation at two strain rates, $\dot{\epsilon} = 1 \times 10^{-7}$ fs^{-1} and $\dot{\epsilon} = 5 \times 10^{-7}$ fs^{-1}. Both cases give a similar value of the maximum K_I around 1.05 MPa m$^{1/2}$. Note that the strain rate less than 5×10^{-7} fs^{-1} also causes minor difference in the stress–strain curve (Fig. 4). Fig. 28 presents the effect of molecular structural anisotropy of clay on K_I. The anisotropy effect is remarkable in that the pyrophyllite sheet shows a greater maximum stress intensity factor under tension in the x direction ($K_I = 1.02$ MPa m$^{1/2}$) than in the y direction ($K_I = 0.9$ MPa m$^{1/2}$). The greater fracture resistance of clay along the x direction agrees with the greater ultimate strength in the same direction as shown in Fig. 7.

Next, we show that our numerical result of fracture toughness is comparable with the data in the literature. Spray (2010) reported that the fracture toughness of phyllosilicate micas is 0.2 MPa m$^{1/2}$ (Obreimoff, 1930), which is about 5 times smaller than our data. This discrepancy may be due to the heterogeneity and anisotropy of the tested specimen (Spray, 1992). Liu (2015) measured fracture toughness

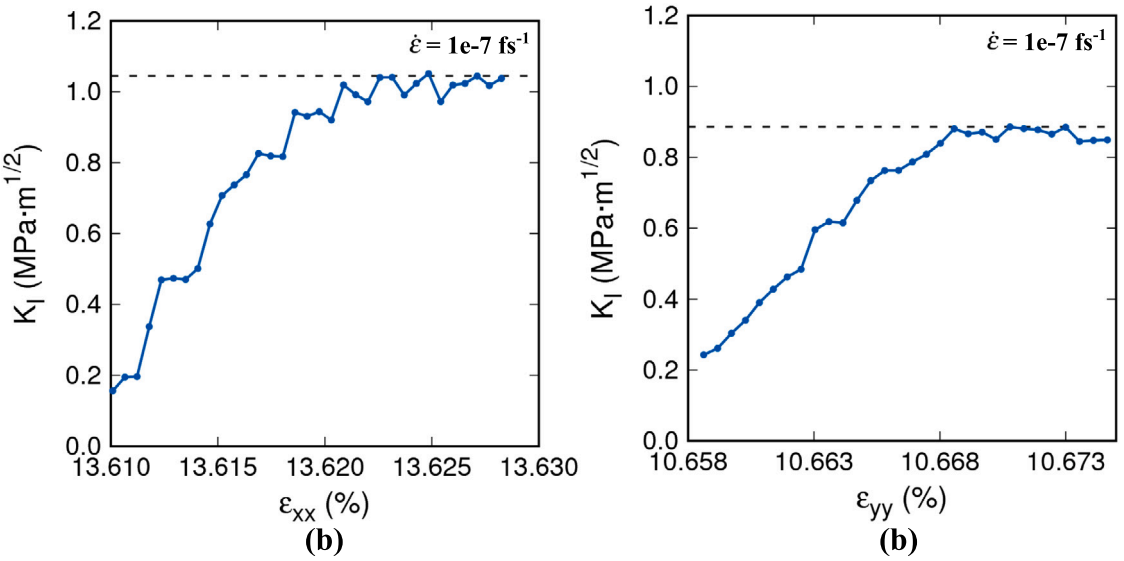

Fig. 28. Stress intensity factor of clay sheet under tensile loading (mode I crack) in (a) x-direction and (b) y-direction at strain rate 1×10^{-7} fs^{-1}.

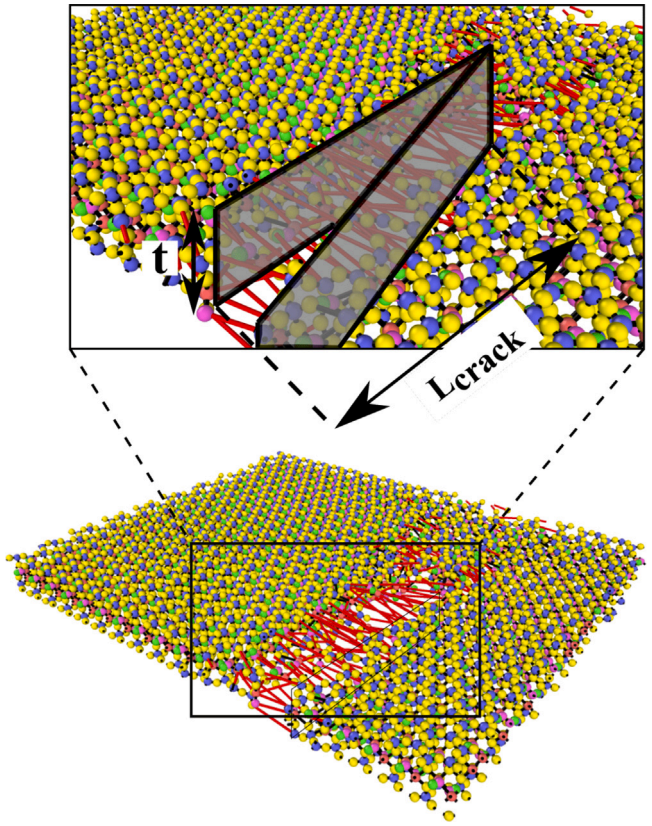

Fig. 29. Schematic of the crack surface under tensile loading in the x direction at ϵ_{xx} = 13.6242%.

in clay shale through nanoindentation tests. The calculated values of fracture toughness for Opalinus clay vary between 0.316 and 0.698 MPa m$^{1/2}$ based on the crack length measurement method while the energy approach gives the values ranging from 0.72 to 1.62 MPa m$^{1/2}$. Hantal et al. (2014) calculated K_{IC} as 0.61 MPa m$^{1/2}$ for cracking across the clay platelet (orthogonal to the 001 plane) through MD simulations with a reactive force field. It is noted that the fracture toughness for cracking between clay sheets (parallel to the 001 plane) is 0.12 MPa m$^{1/2}$, which is not considered in the present study. The fracture toughness of clay sheets obtained from our MD simulations is between 0.9 MPa m$^{1/2}$ and 1.02 MPa m$^{1/2}$. This range is close to the values reported in the aforementioned literature. However, there is a discrepancy between our results and the data reported in the literature. For instance, our results are slightly larger than the value of fracture toughness of the cracking across clay sheets in Hantal et al. (2014). This discrepancy could be due to multiscale issues as discussed in Introduction. Therefore, a multiscale approach would be necessary to model cracks in clay.

3.5. Energy release rate of crack propagation

In this part, we study the energy release rate of crack propagation in the clay sheet at the nanoscale. Griffith (1921) proposed the Griffith energy balance for an incremental increase in crack area, $d\mathscr{A}$, under equilibrium conditions

$$\frac{d\mathscr{E}}{d\mathscr{A}} = \frac{d\mathscr{U}}{d\mathscr{A}} + \frac{d\mathscr{W}}{d\mathscr{A}} = 0, \tag{9}$$

where $\mathscr{E}$ is the total energy, $\mathscr{U}$ is the potential energy, $\mathscr{W}$ is the work required for crack growth, and $\mathscr{A}$ is the crack area. Irwin (1956) defined an energy release rate as the loss of total potential energy per incremental increase in crack area

$$\mathscr{G} = -\frac{d\mathscr{U}}{d\mathscr{A}}. \tag{10}$$

The energy-based approach for fracture propagation is essentially equivalent to the Griffith model. The term "rate" does not refer to the time derivative but the rate of change in potential energy with crack area (Anderson, 2017). The Eqs. (9) and (10) have been successfully used to calculate energy release rates via MD simulations of several materials (e.g., Kikuchi et al., 2005; Jung et al., 2015; Liu et al., 2016; Bao et al., 2018). Thus, in this study we obtain the energy release rate of the pyrophyllite sheet during crack propagation by Eq. (10). The potential energy is obtained from MD simulations and the crack surface area is determined through post-processing.

For simplicity, we assume an edge crack in pyrophyllite and Eq. (10) can be written as

$$\mathscr{G} = -\frac{d\mathscr{U}}{2\mathscr{T}\mathscr{L}_{crack}}, \tag{11}$$

where $\mathscr{T}$ is the thickness of pyrophyllite and $\mathscr{L}_{crack}$ is the crack length. The factor 2 stands for the two surfaces of the crack. Fig. 29 shows the crack surface of the edge crack in clay at ϵ_{xx} = 13.6242%. We calculate

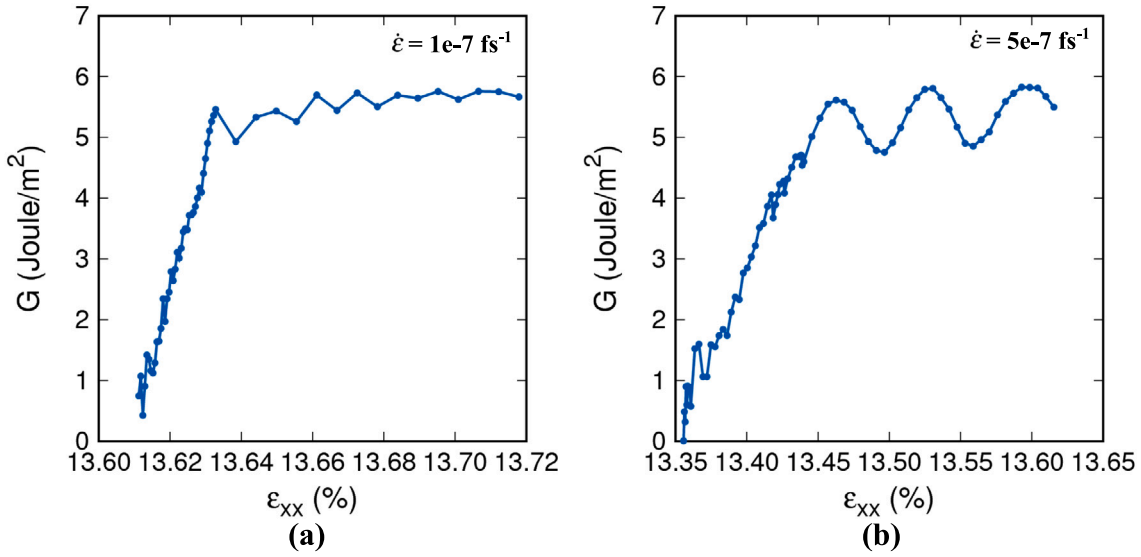

Fig. 30. Energy release rate under tensile loading in the x direction at strain rates (a) 1×10^{-7} fs^{-1} and (b) 5×10^{-7} fs^{-1}.

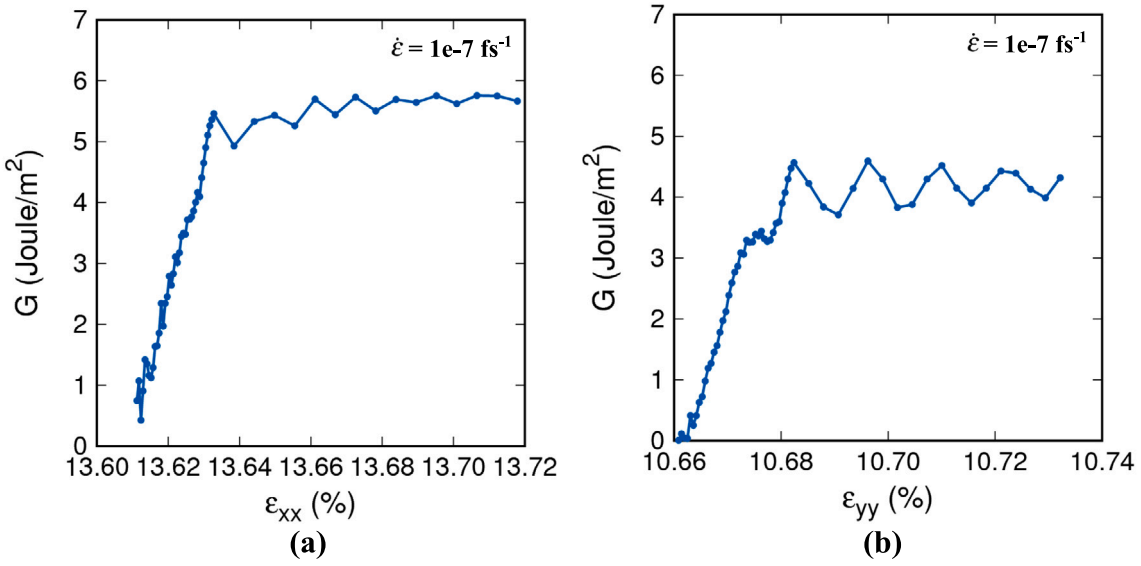

Fig. 31. Energy release rate under tensile loading in (a) x-direction and (b) y-direction at the same strain rate 1×10^{-7} fs^{-1}.

the change in potential energy between the initial configuration and the fully cracked clay at strain rate 1×10^{-7} fs^{-1}. For a flawless clay sheet, the change in crack surface area is equivalent to the area of the crack surface in the clay sheet.

For the case of a pre-existing crack, the critical energy release rate is calculated at the critical moment when the crack is about to propagate from its initial state. For the flawless material in our work, however, the energy release rate first increases from zero with crack growth and then reaches the dynamic equilibrium. Thus, we report the equilibrium energy release rate and compare them at different loading conditions. Fig. 30 compares the energy release rates at two strain rates, $\dot{\epsilon} = 1 \times 10^{-7}$ fs^{-1} and 5×10^{-7} fs^{-1}, during crack propagation under tensile loading in the x direction. The results show a minor strain rate effect on the equilibrium energy release rate. This finding may imply that the strain rate less than $\dot{\epsilon} = 5 \times 10^{-7}$ fs^{-1} could play a negligible role in energy release rates in this study. We also investigate the impact of molecular structural anisotropy on the energy release rate of pyrophyllite. Fig. 31 shows the variation of $\mathscr{G}$ under tensile loading in the x direction and y direction, respectively, at the same strain rate 1×10^{-7} fs^{-1}. The equilibrium energy release rate $\mathscr{G}$ is about 4 Joule/m^2 under tensile loading in the y direction while $\mathscr{G}$ is about 5.5 Joule/m^2 for tensile loading in the x direction. To validate our numerical result, we compare the critical energy release rate with data in the literature. In our simulation, the critical energy release rate of clay under tension is between 4 Joule/m^2 and 5.5 Joule/m^2. This range is on the same order of 3.86 Joule/m^2 reported in the literature (Hantal et al., 2014).

4. Closure

We have studied the atomic-scale mechanism of crack nucleation and growth in dry pyrophyllite sheets through full-scale MD simulations with a general clay force field. The nucleation and propagation of cracks in clay sheets are modeled under both tensile and shear loading conditions. The numerical results show that the cracking in clay sheets under tensile and shear loading could be brittle. The fracture mechanism is investigated from bond breakage analyses at the atomic scale using the notion of critical bond stretch. The number and percentage of different types of broken bonds are presented to probe the atomic-scale mechanism during the cracking process. We have studied the

stress intensity factor and energy release rate of pyrophyllite sheets under tensile loading (mode I crack). Our numerical results of fracture toughness and energy release rate of clay sheets are validated against the data in the literature. This study is focused on understanding the atomic-scale mechanism of the formation of cracks in dry clay sheets under tensile and shear loading. The present work has the potential to provide a nanoscale physics foundation for modeling cracks in clay across time and space through developing a physics-based multiscale modeling technique (e.g., Wagner and Liu, 2003; Xiao and Belytschko, 2004), which is an ongoing research effort.

CRediT authorship contribution statement

Zhe Zhang: Conceptualization, Methodology, Investigation, Writing – original draft. **Xiaoyu Song:** Supervision, Conceptualization, Methodology, Investigation, Writing – review & editing.

Declaration of competing interest

The authors declare the following financial interests/personal relationships which may be considered as potential competing interests: Xiaoyu Song reports financial support was provided by National Science Foundation.

Data availability

No data was used for the research described in the article.

Acknowledgments

This work has been supported by the US National Science Foundation under contract numbers 1659932 and 1944009. We thank the two anonymous reviewers for their expert reviews of this article.

References

Abraham, F.F., Brodbeck, D., Rudge, W.E., Xu, X., 1997. A molecular dynamics investigation of rapid fracture mechanics. J. Mech. Phys. Solids 45 (9), 1595–1619.
Akono, A.T., Kabir, P., 2016. Microscopic fracture characterization of gas shale via scratch testing. Mech. Res. Commun. 78, 86–92.
Allen, M.P., Tildesley, D.J., 2017. Computer Simulation of Liquids. Oxford University Press.
Alonso, E.E., 2021. Triggering and motion of landslides. Géotechnique 71 (1), 3–59.
Anderson, T.L., 2017. Fracture Mechanics: Fundamentals and Applications. CRC Press.
Ayad, R., Konrad, J.M., Soulié, M., 1997. Desiccation of a sensitive clay: application of the model CRACK. Can. Geotech. J. 34 (6), 943–951.
Bao, H., Huang, Y., Yang, Z., Sun, Y., Bai, Y., Miao, Y., Chu, P.K., Xu, K., Ma, F., 2018. Molecular dynamics simulation of nanocrack propagation in single-layer MoS2 nanosheets. J. Phys. Chem. C 122 (2), 1351–1360.
Bitzek, E., Kermode, J.R., Gumbsch, P., 2015. Atomistic aspects of fracture. Int. J. Fract. 191 (1–2), 13–30.
Clausius, R., 1870. XVI. On a mechanical theorem applicable to heat. London, Edinb. Dublin Philos. Mag. J. Sci. 40 (265), 122–127.
Cygan, R.T., Liang, J.J., Kalinichev, A.G., 2004. Molecular models of hydroxide, oxyhydroxide, and clay phases and the development of a general force field. J. Phys. Chem. B 108 (4), 1255–1266.
Duque-Redondo, E., Manzano, H., Epelde-Elezcano, N., Martinez-Martinez, V., Lopez-Arbeloa, I., 2014. Molecular forces governing shear and tensile failure in clay-dye hybrid materials. Chem. Mater. 26 (15), 4338–4345.
Ebrahimi, D., Pellenq, R.J.M., Whittle, A.J., 2012. Nanoscale elastic properties of montmorillonite upon water adsorption. Langmuir 28 (49), 16855–16863.
Frenkel, D., Smit, B., 2001. Understanding Molecular Simulation: From Algorithms to Applications, Vol. 1. Elsevier.
Fu, Y.T., Zartman, G.D., Yoonessi, M., Drummy, L.F., Heinz, H., 2011. Bending of layered silicates on the nanometer scale: mechanism, stored energy, and curvature limits. J. Phys. Chem. C 115 (45), 22292–22300.
Gereben, O., Petkov, V., 2013. Reverse Monte Carlo study of spherical sample under non-periodic boundary conditions: the structure of ru nanoparticles based on x-ray diffraction data. J. Phys.: Condens. Matter 25 (45), 454211.
Griffith, A.A., 1921. VI. The phenomena of rupture and flow in solids. Philos. Trans. R. Soc. London. Ser. A, Containing Papers A Math. Phys. Character 221 (582–593), 163–198.
Hallett, P., Newson, T., 2001. A simple fracture mechanics approach for assessing ductile crack growth in soil. Soil Sci. Am. J. 65 (4), 1083–1088.
Han, J., Sohn, D., Woo, W., Kim, D.K., 2017. Molecular dynamics study of fracture toughness and trans-intergranular transition in bi-crystalline graphene. Comput. Mater. Sci. 129, 323–331.
Hanson, J.A., Hardin, B.O., Mahboub, K., 1994. Fracture toughness of compacted cohesive soils using ring test. J. Geotech. Eng. 120 (5), 872–891.
Hantal, G., Brochard, L., Laubie, H., Ebrahimi, D., Pellenq, R.J.M., Ulm, F.J., Coasne, B., 2014. Atomic-scale modelling of elastic and failure properties of clays. Mol. Phys. 112 (9–10), 1294–1305.
Hockney, R.W., Eastwood, J.W., 2021. Computer Simulation using Particles. crc Press.
Hoover, W.G., 1985. Canonical dynamics: Equilibrium phase-space distributions. Phys. Rev. A 31 (3), 1695.
Irwin, G.R., 1956. Onset of Fast Crack Propagation in High Strength Steel and Aluminum Alloys. Technical Report, Naval Research Lab Washington DC.
Jia, X., Hao, Y., Li, P., Zhang, X., Lu, D., 2021. Nanoscale deformation and crack processes of kaolinite under water impact using molecular dynamics simulations. Appl. Clay Sci. 206, 106071.
Jung, G., Qin, Z., Buehler, M.J., 2015. Molecular mechanics of polycrystalline graphene with enhanced fracture toughness. Extreme Mech. Lett. 2, 52–59.
Kikuchi, H., Kalia, R.K., Nakano, A., Vashishta, P., Branicio, P.S., Shimojo, F., 2005. Brittle dynamic fracture of crystalline cubic silicon carbide (3C-SiC) via molecular dynamics simulation. J. Appl. Phys. 98 (10), 103524.
Kodikara, J., Barbour, S., Fredlund, D., 2020. Desiccation cracking of soil layers. In: Unsaturated Soils for Asia. CRC Press, pp. 693–698.
Lambe, T.W., Whitman, R.V., 1991. Soil Mechanics, Vol. 10. John Wiley & Sons.
Le, M.Q., Batra, R.C., 2016. Mode-i stress intensity factor in single layer graphene sheets. Comput. Mater. Sci. 118, 251–258.
Lee, J.H., Guggenheim, S., 1981. Single crystal X-ray refinement of pyrophyllite-1 Tc. Am. Mineral. 66 (3–4), 350–357.
Li, J., Li, L., Chen, R., Li, D., 2016. Cracking and vertical preferential flow through landfill clay liners. Eng. Geol. 206, 33–41.
Likos, W.J., Song, X., Xiao, M., Cerato, A., Lu, N., 2019. Fundamental challenges in unsaturated soil mechanics. In: Geotechnical Fundamentals for Addressing New World Challenges. Springer, pp. 209–236.
Lisjak, A., Grasselli, G., Vietor, T., 2014. Continuum–discontinuum analysis of failure mechanisms around unsupported circular excavations in anisotropic clay shales. Int. J. Rock Mech. Min. Sci. 65, 96–115.
Liu, Y., 2015. Fracture toughness assessment of shales by nanoindentation.
Liu, N., Hong, J., Pidaparti, R., Wang, X., 2016. Fracture patterns and the energy release rate of phosphorene. Nanoscale 8 (10), 5728–5736.
Lu, N., Dong, Y., 2017. Correlation between soil-shrinkage curve and water-retention characteristics. J. Geotech. Geoenviron. Eng. 143 (9), 04017054.
Lu, N., Godt, J.W., 2013. Hillslope Hydrology and Stability. Cambridge University Press.
Lu, N., Kaya, M., 2013. A drying cake method for measuring suction-stress characteristic curve, soil–water-retention curve, and hydraulic conductivity function. Geotech. Test. J. 36 (1), 1–19.
Maxwell, J.C., 1870. I.—on reciprocal figures, frames, and diagrams of forces. Earth Environ. Sci. Trans. R. Soc. Edinb. 26 (1), 1–40.
Menon, S., Song, X., 2019. Coupled analysis of desiccation cracking in unsaturated soils through a non-local mathematical formulation. Geosciences 9 (10), 428.
Menon, S., Song, X., 2022a. Computational multiphase periporomechanics for unguided cracking in unsaturated porous media. Internat. J. Numer. Methods Engrg. 123 (12), 2837–2871.
Menon, S., Song, X., 2022b. Computational coupled large-deformation periporomechanics for dynamic failure and fracturing in variably saturated porous media. Internat. J. Numer. Methods Engrg. 1–39. http://dx.doi.org/10.1002/nme.7109.
Militzer, B., Wenk, H.R., Stackhouse, S., Stixrude, L., 2011. First-principles calculation of the elastic moduli of sheet silicates and their application to shale anisotropy. Am. Mineral. 96 (1), 125–137.
Miller, C.J., Mi, H., Yesiller, N., 1998. Experimental analysis of desiccation crack propagation in clay liners 1. JAWRA J. Am. Water Resour. Assoc. 34 (3), 677–686.
Mitchell, J.K., Soga, K., 2005. Fundamentals of Soil Behavior, Vol. 3. John Wiley & Sons New York.
Niu, W.J., Ye, W.M., Song, X., 2020. Unsaturated permeability of gaomiaozi bentonite under partially free-swelling conditions. Acta Geotech. 15 (5), 1095–1124.
Obreimoff, J., 1930. The splitting strength of mica. Proc. R. Soc. London. Ser. A, Containing Papers A Math. Phys. Character 127 (805), 290–297.
Ortega, J.A., Ulm, F.J., Abousleiman, Y., 2007. The effect of the nanogranular nature of shale on their poroelastic behavior. Acta Geotech. 2 (3), 155–182.
Plimpton, S., 1995. Fast parallel algorithms for short-range molecular dynamics. J. Comput. Phys. 117 (1), 1–19.
Pouvreau, M., Greathouse, J.A., Cygan, R.T., Kalinichev, A.G., 2019. Structure of hydrated kaolinite edge surfaces: DFT results and further development of the ClayFF classical force field with metal–O–H angle bending terms. J. Phys. Chem. C 123 (18), 11628–11638.
Rycroft, C., 2009. Voro++: A Three-Dimensional Voronoi Cell Library in C++. Technical Report, Lawrence Berkeley National Lab.(LBNL), Berkeley, CA (United States).
Song, X., Wang, M.C., 2019. Molecular dynamics modeling of a partially saturated clay-water system at finite temperature. Int. J. Numer. Anal. Methods Geomech. 43 (13), 2129–2146.

Song, X., Wang, M.-C., Zhang, K., 2018. Molecular dynamics modeling of unsaturated clay-water systems at elevated temperature. In: The 7th International Conference on Unsaturated Soils 2018 (UNSAT2018)-Ng, Leung, Chiu & Zhou (Eds) the Hong Kong University of Science and Technology, ISBN 978-988-78037-3-7.

Song, X., Zhang, Z., 2021. Determination of clay-water contact angle via molecular dynamics and deep-learning enhanced methods. Acta Geotech. 1–15.

Spray, J.G., 1992. A physical basis for the frictional melting of some rock-forming minerals. Tectonophysics 204 (3–4), 205–221.

Spray, J.G., 2010. Frictional melting processes in planetary materials: From hypervelocity impact to earthquakes. Annu. Rev. Earth Planet. Sci. 38, 221–254.

Stukowski, A., 2009. Visualization and analysis of atomistic simulation data with OVITO–the open visualization tool. Modelling Simulation Mater. Sci. Eng. 18 (1), 015012.

Subramaniyan, A.K., Sun, C., 2008. Continuum interpretation of virial stress in molecular simulations. Int. J. Solids Struct. 45 (14–15), 4340–4346.

Teich-McGoldrick, S.L., Greathouse, J.A., Cygan, R.T., 2012. Molecular dynamics simulations of structural and mechanical properties of muscovite: pressure and temperature effects. J. Phys. Chem. C 116 (28), 15099–15107.

Terzaghi, K., Peck, R.B., Mesri, G., 1996. Soil Mechanics in Engineering Practice. John Wiley & Sons.

Thusyanthan, N., Take, W., Madabhushi, S., Bolton, M., 2007. Crack initiation in clay observed in beam bending. Geotechnique 57 (7), 581–594.

Van Duin, A.C., Dasgupta, S., Lorant, F., Goddard, W.A., 2001. Reaxff: A reactive force field for hydrocarbons. J. Phys. Chem. A 105 (41), 9396–9409.

Vanommeslaeghe, K., Hatcher, E., Acharya, C., Kundu, S., Zhong, S., Shim, J., Darian, E., Guvench, O., Lopes, P., Vorobyov, I., et al., 2010. CHARMM general force field: A force field for drug-like molecules compatible with the CHARMM all-atom additive biological force fields. J. Comput. Chem. 31 (4), 671–690.

Wagner, G.J., Liu, W.K., 2003. Coupling of atomistic and continuum simulations using a bridging scale decomposition. J. Comput. Phys. 190 (1), 249–274.

Wang, Z., Wang, H., Cates, M.E., 2001. Effective elastic properties of solid clays. Geophysics 66 (2), 428–440.

Wardle, R., Brindley, G., 1972. The crystal structures of pyrophyllite, 1Te, and of its dehydroxylate. Am. Mineral.: J. Earth Planet. Mater. 57 (5–6), 732–750.

Xiao, S., Belytschko, T., 2004. A bridging domain method for coupling continua with molecular dynamics. Comput. Methods Appl. Mech. Engrg. 193 (17–20), 1645–1669.

Yang, G., Neretnieks, I., Holmboe, M., 2017. Atomistic simulations of cation hydration in sodium and calcium montmorillonite nanopores. J. Chem. Phys. 147 (8), 084705.

Zartman, G.D., Liu, H., Akdim, B., Pachter, R., Heinz, H., 2010. Nanoscale tensile, shear, and failure properties of layered silicates as a function of cation density and stress. J. Phys. Chem. C 114 (4), 1763–1772.

Zhang, Z., Song, X., 2021. Characterizing the impact of temperature on clay-water contact angle in geomaterials during extreme events by deep learning enhanced method. In: Geo-Extreme 2021. pp. 160–168.

Zhang, Z., Song, X., 2022. Nonequilibrium molecular dynamics (NEMD) modeling of nanoscale hydrodynamics of clay-water system at elevated temperature. Int. J. Numer. Anal. Methods Geomech. 1–22. http://dx.doi.org/10.1002/nag.3325.

Zhang, L.L., Zheng, Y.Y., Wei, P.C., Diao, Q.F., Yin, Z.Y., 2021. Nanoscale mechanical behavior of kaolinite under uniaxial strain conditions. Appl. Clay Sci. 201, 105961.

Zhou, X., Zimmerman, J., Reedy Jr., E., Moody, N., 2008. Molecular dynamics simulation based cohesive surface representation of mixed mode fracture. Mech. Mater. 40 (10), 832–845.

Zimmerman, J.A., WebbIII, E.B., Hoyt, J., Jones, R.E., Klein, P., Bammann, D.J., 2004. Calculation of stress in atomistic simulation. Modelling Simulation Mater. Sci. Eng. 12 (4), S319.